

## LIGHT CURVE TEMPLATES AND GALACTIC DISTRIBUTION OF RR LYRAE STARS FROM SLOAN DIGITAL SKY SURVEY STRIPE 82

BRANIMIR SESAR<sup>1</sup>, ŽELJKO IVEZIĆ<sup>1</sup>, SKYLER H. GRAMMER<sup>1</sup>, DYLAN P. MORGAN<sup>1</sup>, ANDREW C. BECKER<sup>1</sup>, MARIO JURIC<sup>2</sup>,  
NATHAN DE LEE<sup>3</sup>, JAMES ANNIS<sup>4</sup>, TIMOTHY C. BEERS<sup>5</sup>, XIAOHUI FAN<sup>6</sup>, ROBERT H. LUPTON<sup>7</sup>, JAMES E. GUNN<sup>7</sup>,  
GILLIAN R. KNAPP<sup>7</sup>, LINHUA JIANG<sup>6</sup>, SEBASTIAN JESTER<sup>8</sup>, DAVID E. JOHNSTON<sup>7</sup>, AND HUBERT LAMPEITL<sup>4</sup>

<sup>1</sup> University of Washington, Department of Astronomy, P.O. Box 351580, Seattle, WA 98195-1580, USA

<sup>2</sup> Institute for Advanced Study, 1 Einstein Drive, Princeton, NJ 08540, USA

<sup>3</sup> University of Florida, Department of Astronomy, P.O. Box 112055, Gainesville, FL 32611-2055, USA

<sup>4</sup> Fermi National Accelerator Laboratory, P.O. Box 500, Batavia, IL 60510, USA

<sup>5</sup> Michigan State University, Department of Physics & Astronomy, and JINA: Joint Institute for Nuclear Astrophysics, East Lansing, MI 48824-2320, USA

<sup>6</sup> Steward Observatory, University of Arizona, Tucson, AZ 85721-0065, USA

<sup>7</sup> Princeton University Observatory, Princeton, NJ 08544-1001, USA

<sup>8</sup> Max-Planck-Institut für Astronomie, Königstuhl 17, D-69117 Heidelberg, Germany

Received 2009 July 30; accepted 2009 November 12; published 2009 December 15

### ABSTRACT

We present an improved analysis of halo substructure traced by RR Lyrae stars in the Sloan Digital Sky Survey (SDSS) stripe 82 region. With the addition of SDSS-II data, a revised selection method based on new *ugriz* light curve templates results in a sample of 483 RR Lyrae stars that is essentially free of contamination. The main result from our first study persists: the spatial distribution of halo stars at galactocentric distances 5–100 kpc is highly inhomogeneous. At least 20% of halo stars within 30 kpc from the Galactic center can be statistically associated with substructure. We present strong direct evidence, based on both RR Lyrae stars and main-sequence stars, that the halo stellar number density profile significantly steepens beyond a Galactocentric distance of  $\sim 30$  kpc, and a larger fraction of the stars are associated with substructure. By using a novel method that simultaneously combines data for RR Lyrae and main-sequence stars, and using photometric metallicity estimates for main-sequence stars derived from deep co-added *u*-band data, we measure the metallicity of the Sagittarius dSph tidal stream (trailing arm) toward R.A.  $\sim 2^{\text{h}}\text{--}3^{\text{h}}$  and decl.  $\sim 0^{\circ}$  to be 0.3 dex higher ( $[\text{Fe}/\text{H}] = -1.2$ ) than that of surrounding halo field stars. Together with a similar result for another major halo substructure, the Monoceros stream, these results support theoretical predictions that an early forming, smooth inner halo, is metal-poor compared to high surface brightness material that have been accreted onto a later-forming outer halo. The mean metallicity of stars in the outer halo that are not associated with detectable clumps may still be more metal-poor than the bulk of inner-halo stars, as has been argued from other data sets.

*Key words:* Galaxy: halo – Galaxy: stellar content – Galaxy: structure – methods: data analysis – stars: horizontal-branch – stars: statistics – stars: variables: other

*Online-only material:* color figures, figure set, machine-readable tables, animation, supplementary data

### 1. INTRODUCTION

Studies of the Galactic halo can help constrain the formation history of the Milky Way and the galaxy formation process in general. For example, within the framework of hierarchical galaxy formation (Freeman & Bland-Hawthorn 2002), the spheroidal component of the luminous matter should reveal substructures such as tidal tails and streams (Johnston et al. 1996; Helmi & White 1999; Bullock et al. 2001; Harding et al. 2001). The number of these substructures, due to mergers and accretion over the Galaxy’s lifetime, may provide a crucial test for proposed solutions to the “missing satellite” problem (Bullock et al. 2001). Substructures are expected to be ubiquitous in the outer halo (galactocentric distance  $> 15\text{--}20$  kpc), where the dynamical timescales are sufficiently long for them to remain spatially coherent (Johnston et al. 1996; Mayer et al. 2002), and indeed many have been discovered (e.g., Ibata et al. 1997; Yanny et al. 2000; Ivezić et al. 2000; Belokurov et al. 2006, 2007a; Grillmair 2006; Vivas & Zinn 2006; Newberg et al. 2007; Jurić et al. 2008). Various luminous tracers, such as main-sequence turnoff (MSTO) stars, RR Lyrae variables, or red giants, are used to detect halo substructures, and of them, RR Lyrae stars have proven to be especially useful.

RR Lyrae stars represent a fair sample of the old halo population (Smith 1995). They are nearly standard candles ( $\langle M_V \rangle = 0.59 \pm 0.03$  at  $[\text{Fe}/\text{H}] = -1.5$ ; Cacciari & Clementini 2003), are sufficiently bright to be detected at large distances (5–120 kpc for  $14 < V < 21$ ), and are sufficiently numerous to trace the halo substructure with good spatial resolution ( $\sim 1.5$  kpc at 30 kpc). Fairly complete and relatively clean samples of RR Lyrae stars can be selected using single-epoch colors (Ivezić et al. 2005), and if multi-epoch data exist, using variability (Ivezić et al. 2000; QUEST, Vivas et al. 2001; Sesar et al. 2007; De Lee 2008; SEKBO, Keller et al. 2008; LONEOS-I, Miceli et al. 2008). A useful comparison of recent RR Lyrae surveys in terms of their sky coverage, distance limits, and sample size is presented by Keller et al. (2008, see their Table 1). Compared to other surveys, the so-called stripe 82 survey (an equatorial strip defined by declination limits of  $\pm 1^{\circ}27'$  and extending from R.A.  $\sim 20^{\text{h}}$  to R.A.  $\sim 4^{\text{h}}$ ) based on Sloan Digital Sky Survey (SDSS) data (York et al. 2000) is the deepest one yet obtained (probing distances to  $\sim 110$  kpc), and the only survey with available five-band photometry.

In an initial study based on SDSS stripe 82 data, we discovered a complex spatial distribution of halo RR Lyrae stars at

distances ranging from 5 kpc to  $\sim 100$  kpc (Sesar et al. 2007, hereafter S07). The candidate RR Lyrae sample was selected using colors and low-order light curve statistics. In this paper, we present a full light curve analysis enabled by the addition of new stripe 82 observations. The resulting sample of RR Lyrae stars is highly complete and essentially free of contamination. The extended observations now allow the determination of flux-averaged magnitudes, thus providing better luminosity and distance estimates. This reduces the uncertainty in the spatial distribution of RR Lyrae stars, and increases the overall accuracy of computed density maps.

While this paper was in preparation, another study of RR Lyrae stars in stripe 82, based on essentially the same data set, was announced (Watkins et al. 2009). In addition to analysis that overlaps with their work, here we also discuss the following.

1. An RR Lyrae template construction for the SDSS bandpasses, and analysis of the template behavior.
2. Template fitting and visual inspection of best fits for single-band and color light curves, which results in an exceedingly clean final sample.
3. Extended color range for the initial selection, which results in about 20% more stars than in the sample analyzed by Watkins et al.
4. A step-by-step analysis of the sample incompleteness at the faint end.
5. A new method for constraining the metallicity of spatially coherent structures that are detected using main-sequence and RR Lyrae stars.
6. A comparison of the observed RR Lyrae spatial distribution with predictions based on an oblate halo model constrained by SDSS observations of main-sequence stars.

We emphasize, however, that both studies obtain consistent main results: strong substructure in the spatial distribution of halo RR Lyrae stars and evidence for a steepening of the best-fit power-law description beyond a galactocentric radius of  $\sim 30$  kpc.

Our data set and the initial selection of candidate RR Lyrae stars are described in Section 2, while the construction of light curve templates is presented in Section 3. Various properties of the resulting RR Lyrae sample, with emphasis on the spatial distribution, are analyzed in Section 4. In Section 5, we compare the spatial distribution of RR Lyrae stars and main-sequence stars and constrain the metallicity distribution of the Sgr tidal stream. Our main results are summarized and discussed in Section 6.

## 2. THE DATA

### 2.1. An Overview of the SDSS Imaging and Stripe 82 Data

The SDSS (Adelman-McCarthy et al. 2008) provides homogeneous and deep ( $r < 22.5$ ) photometry in five bands ( $u$ ,  $g$ ,  $r$ ,  $i$ , and  $z$ ) of more than  $7500 \text{ deg}^2$  of the North Galactic Cap, and three stripes in the South Galactic Cap totaling  $740 \text{ deg}^2$ . The central stripe in the South Galactic Cap, stripe 82 ( $20^{\text{h}}32^{\text{m}} < \alpha_{\text{J2000.0}} < 04^{\text{h}}00^{\text{m}}$ ,  $-1^{\circ}26 < \delta_{\text{J2000.0}} < +1^{\circ}26$ ,  $\sim 280 \text{ deg}^2$ ) was observed repeatedly (not all imaging runs cover the entire region) to enable a deep co-addition of the data and to enable the discovery of variable objects. It was the largest source of multi-epoch data during the first phase of the SDSS (SDSS-I), with a median of 10–20 observations per source (S07; Bramich et al. 2008) and it remains so thanks to additional imaging runs obtained during the SDSS-II Supernova (SN) survey

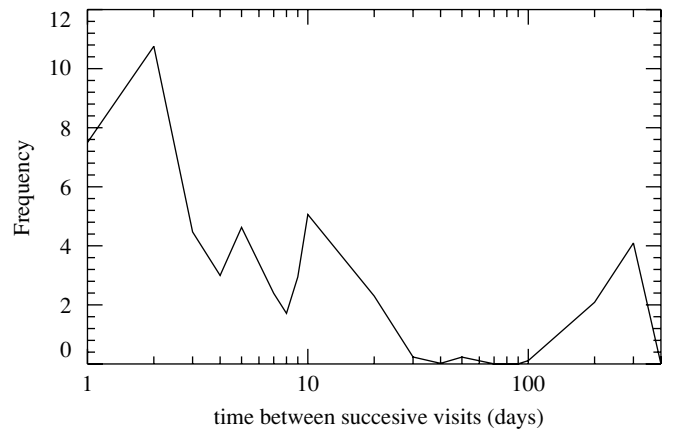


**Figure 1.** Cadence of SDSS stripe 82 observations. On average, the objects were most often re-observed every two days (the SDSS-II SN Survey cadence), followed by 5-day, 10-day, and yearly re-observations.

(Frieman et al. 2008). Some of the SDSS-II SN imaging runs were taken in bad photometric conditions (e.g., with fast-changing cloud coverage), rendering the photometric data unreliable if not recalibrated. We have followed the Ivezić et al. (2007) prescription (see their Section 3) and recalibrated 180 SDSS-II imaging runs to 1% photometry (magnitude zero-point uncertainty  $\lesssim 0.01$  mag). The repeated photometric measurements demonstrate that the photometric precision is about 0.02 mag at the bright end and reaches 0.05 mag at magnitudes of 20, 21.5, 21.5, 21.5, and 19 for the  $ugriz$  bands, respectively (S07). The morphological information from the images allows reliable star–galaxy separation to  $r \sim 21.5$  (Lupton et al. 2002).

We have combined SDSS-I imaging runs used in S07 with recalibrated SDSS-II SN imaging runs, and created a catalog with  $\sim 4.4$  million unique unresolved (point source) objects. Each object in the catalog was observed at least four times in the  $ugr$  bands, and the cadence of re-observations is shown in Figure 1. On average, the SDSS stripe 82 objects were most often re-observed every two days (the SDSS-II SN Survey cadence), followed by 5 day, 10 day, and yearly re-observations. We time-average repeated  $ugriz$  observations (median point-spread function magnitudes) and correct them for interstellar extinction using the map from Schlegel et al. (1998). We also compute various low-order statistics, such as the rms scatter ( $\sigma$ ),  $\chi^2$  per degree of freedom ( $\chi^2$ ), and light-curve skewness ( $\gamma$ ) for each  $ugriz$  band and each object (see S07 for details). For objects brighter than  $g = 21$ , the median number of observations per band is 30.

The constructed catalog is a superb data set for the selection and identification of RR Lyrae stars. The three-fold increase in the median number of observations per object over the S07 catalog allows a reliable measurement of the period of pulsation and enables the construction of period-folded  $ugriz$  light curves. As we describe in the following section, RR Lyrae stars can be unambiguously identified using their period-folded  $ugriz$  light curves, and an essentially complete sample of stripe 82 RR Lyrae stars can then be constructed.

### 2.2. The Selection of RR Lyrae Stars

In this section, we describe the selection of 483 RR Lyrae stars in SDSS stripe 82. The positions and photometry (MJD,  $ugriz$  magnitudes, and errors) of selected RR Lyrae stars are provided in the supplementary data file available in the electronic edition of the journal; the data format is provided in Table 1.

**Table 1**  
Positions and *ugriz* Photometry for Stripe 82 RR Lyrae Stars

R.A. <sup>a</sup>	Decl. <sup>a</sup>	$u_{\text{MJD}}^b$	$u^c$	$u_{\text{err}}^d$	$g_{\text{MJD}}^b$	$g^c$	$g_{\text{err}}^d$	$r_{\text{MJD}}^b$	$r^c$	$r_{\text{err}}^d$	$i_{\text{MJD}}^b$	$i^c$	$i_{\text{err}}^d$	$z_{\text{MJD}}^b$	$z^c$	$z_{\text{err}}^d$
0.935679	1.115859	51075.3024	18.04	0.01	51075.3041	16.79	0.01	51075.3007	16.65	0.01	51075.3016	16.62	0.01	51075.3032	16.59	0.01
0.935679	1.115859	52196.3030	18.54	0.02	52196.3047	17.35	0.01	52196.3013	17.05	0.01	52196.3022	16.94	0.01	52196.3038	16.88	0.01
0.935679	1.115859	52197.3161	-99.99	-99.00	52197.3178	17.21	0.01	52197.3144	16.89	0.01	52197.3153	16.77	0.01	52197.3169	16.75	0.01
0.935679	1.115859	52225.1663	18.53	0.02	52225.1679	17.34	0.01	52225.1646	17.05	0.01	52225.1654	16.94	0.01	52225.1671	16.90	0.01
0.935679	1.115859	52231.2020	-99.99	-99.00	52231.2037	16.98	0.01	52231.2003	16.77	0.01	52231.2012	16.67	0.01	52231.2029	16.65	0.01

**Notes.** The positions and *ugriz* photometry for all 483 RR Lyra are given in the supplementary data file available in the online edition of the journal.

<sup>a</sup> Median equatorial J2000.0 right ascension and declination in degrees.

<sup>b</sup> Modified Julian date in days.

<sup>c</sup> Magnitude is not corrected for ISM extinction, -99.00 if the measurement is unreliable.

<sup>d</sup> Magnitude uncertainty, -99.00 if the measurement is unreliable.

In S07, we defined color and variability cuts specifically designed for the selection of candidate RR Lyrae stars. We adopt those selection criteria, and expand the probed  $u - g$  color range from  $u - g = 0.98$  (used in S07) to  $u - g = 0.7$ . This expansion is motivated by theoretical predictions obtained from recent RR Lyrae pulsation models by Marconi et al. (2006). They find that, for a given effective temperature, more metal-poor stars have bluer  $u - g$  colors. A similar behavior is also detected in main-sequence stars (Ivezić et al. 2008 and references therein). Thus, the expanded  $u - g$  color range might increase completeness for more metal-poor RR Lyrae stars; at the same time the sample contamination is not an issue because light curves are now well sampled.

We start the RR Lyrae candidate selection by making the following color,

$$0.7 < u - g < 1.35, \quad (1)$$

$$-0.15 < g - r < 0.40, \quad (2)$$

$$-0.15 < r - i < 0.22, \quad (3)$$

$$-0.21 < i - z < 0.25, \quad (4)$$

and variability cuts:

1. the number of  $g$ -band observations,  $N_{\text{obs},g} > 15$ ;
2. the chi-square per degree of freedom in the  $g$  and  $r$  bands,  $\chi^2(g) > 3$  and  $\chi^2(r) > 3$ ;
3. the rms scatter in the  $g$  and  $r$  bands,  $\sigma(g) > 0.05$  mag and  $\sigma(r) > 0.05$  mag;
4. the ratio of the rms scatter in the  $g$  and  $r$  bands,  $0.7 < \sigma(g)/\sigma(r) \leq 2.5$ ; and
5. the  $g$ -band light curve skewness,  $\gamma(g) \leq 1$ , to avoid eclipsing binaries (see S07 for details).

Note that the colors in Equations (1)–(4) are obtained from time-averaged (median) *ugriz* magnitudes, corrected for extinction using the maps from Schlegel et al. (1998). These criteria are designed to reject stars that are definitely not RR Lyrae, and all but one ( $N_{\text{obs},g} > 15$ ) should be satisfied by every true RR Lyrae star. The second variability criterion can introduce incompleteness at the faint end, because photometric errors increase with magnitude. We address this incompleteness effect in detail in Section 4.2. Using these criteria, we select the initial sample of 3449 candidate RR Lyrae stars (about one in seven are true RR Lyrae stars; the fraction of RR Lyrae stars in the full sample is about  $1$  in  $10^4$ ), and proceed to measure their light curve periods in the next step.

To estimate the period of pulsation for candidate RR Lyrae stars, we use an implementation of the *Supersmoother* routine (Reimann 1994). The routine uses a running mean or running linear regression on the data to fit the observations as a function of phase to a range of periods, constrained to be between 0.2 and 1.0 days (see Figure 9 in Eyer & Mowlavi 2008). The main advantage of this routine is that the light curve shape need not be known in advance. We supply the Modified Julian date (MJD) of observations,  $g$ -band magnitudes and their errors, and the routine outputs the first five periods with the lowest chi-square values. The  $g$ -band magnitudes are used instead of  $u$ - or  $r$ -band magnitudes because they have higher signal-to-noise ratios than the  $u$ -band magnitudes, and because RR Lyrae stars have a larger amplitude of variability in the  $g$  band than in the  $r$  band (Ivezić et al. 2000; S07). The precision of periods is about a few seconds, and was determined by comparing periods estimated from  $g$ - and  $r$ -band data.

Using each of the five periods supplied by the *Supersmoother* routine, we period-fold a  $g$ -band light curve and then fit to it one of the eight  $V$ -band template RR Lyrae light curves. The  $V$ -band template light curves were obtained from Layden (1998, six RR type *ab* templates) and K. Vivas (2007, private communication; two RR type *c* templates), and are used due to the lack of  $g$ -band templates in the literature. The fitting is performed in the least-square sense, with the epoch of the maximum brightness  $\phi_0^g$ , peak-to-peak amplitude  $A_g$ , and mean magnitude  $g_0$  as free parameters. The precision of the epoch of maximum brightness is on the order of a few minutes, and was determined by comparing epochs of maximum brightness estimated from  $g$ - and  $r$ -band light curves fitted with  $V$ -band templates.

To robustly quantify the quality of a template fit, we define a  $\chi^2$ -like parameter

$$\zeta = \text{median}(|m_{\text{observed}}^i - m_{\text{template}}^i| / \sigma_{\text{observed}}^i), \quad (5)$$

where  $m_{\text{observed}}$  and  $\sigma_{\text{observed}}$  are the observed magnitude and its uncertainty,  $m_{\text{template}}$  is the magnitude predicted by the template, and  $i = 1, N_{\text{obs}}$ , where  $N_{\text{obs}}$  is the number of observations. Here we use the median to minimize the bias in  $\zeta$  due to poor observations (outliers). The template with the lowest  $\zeta$  value is selected as the best fit, and the best-fit parameters are stored.

Initially, we wanted to use  $\zeta$  to separate RR Lyrae stars from non-RR Lyrae stars. Low  $\zeta$  values, indicating good agreement between the observed light curves (data) and template light curves (models), would indicate that a candidate is an RR Lyrae star. Likewise, high  $\zeta$  values would indicate that a candidate is not an RR Lyrae star. However, visual inspection of light curves initially classified as non-RR Lyrae (high  $\zeta$  values) showed that some of the light curves are actually quite RR Lyrae-like, but

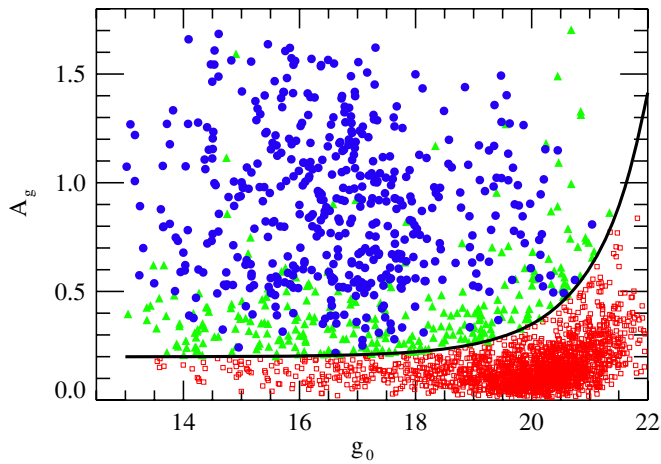


**Figure 2.** Distribution of  $g$ -band amplitudes ( $A_g$ ) and maximum brightness ( $g_0$ ) determined from best-fit templates for 3449 RR Lyrae candidates. The solid line separates candidates into template-accepted (blue dots) and ambiguous candidates (green triangles), which lie above the line, and template-rejected (red open squares) which lie below the line.

(A color version of this figure is available in the online journal.)

with a lot of scatter around the template-predicted values. We suspect that these stars are RR Lyrae stars that undergo changes in their period, light curve shape, or amplitude as a function of time (e.g., the Blazhko effect; Blazhko 1907; Kolenberg 2008). By putting a hard limit on  $\zeta$  such RR Lyrae stars would be rejected, and the completeness of our sample (the fraction of recovered RR Lyrae stars) would decrease. To avoid this, we look for additional criteria beyond the light curve shape that can be used to distinguish true RR Lyrae stars from non-RR Lyrae stars. For this purpose we have created a “training” set of 479 RR Lyrae stars that were selected by visual inspection of their light curves, and use it to explore the variability phase space of RR Lyrae stars. Hereafter we refer to the training set as the template-accepted RR Lyrae stars.

Based on the distribution of template-accepted RR Lyrae stars shown in Figure 2, we define a line that separates candidate RR Lyrae into template-accepted and ambiguous (above the line), and template-rejected candidates below the line). The ambiguous candidates (362 objects) did not have at first visually convincing (RR Lyrae-like) light curves, but based on their variability properties (rms scatter in the  $g$ ,  $r$ , and  $g - r$ ) some of them might be true RR Lyrae stars.

The question of whether some of the ambiguous candidates are true RR Lyrae stars is especially important at the faint end. As shown in Figure 2, the distribution of template-accepted RR Lyrae stars has a sharp cutoff around  $g_0 \sim 20.5$ , suggesting a limit on the spatial distribution of halo stars. A similar cutoff in the distribution of RR Lyrae stars was also discussed by Ivezić et al. (2000). If it can be shown that the ambiguous candidates with  $g_0 \sim 20.5$  have properties (beside their light curves) that are inconsistent with the properties of template-accepted RR Lyrae stars, they could be excluded from the sample, and the claim that the halo cutoff is real would become much stronger.

Aiming to define the RR Lyrae variability space, we now consider how the three groups of candidates distribute in the  $\sigma_g$  versus  $\sigma_r$  diagram, where the  $\sigma_g$  and  $\sigma_r$  are the rms scatter in the  $g$  and  $r$  bands, respectively. This projection of phase space is useful as it separates pulsationally variable stars from other variable sources (S07). As shown in Figure 3 (top), the majority of template-accepted RR Lyrae stars exist in a narrow

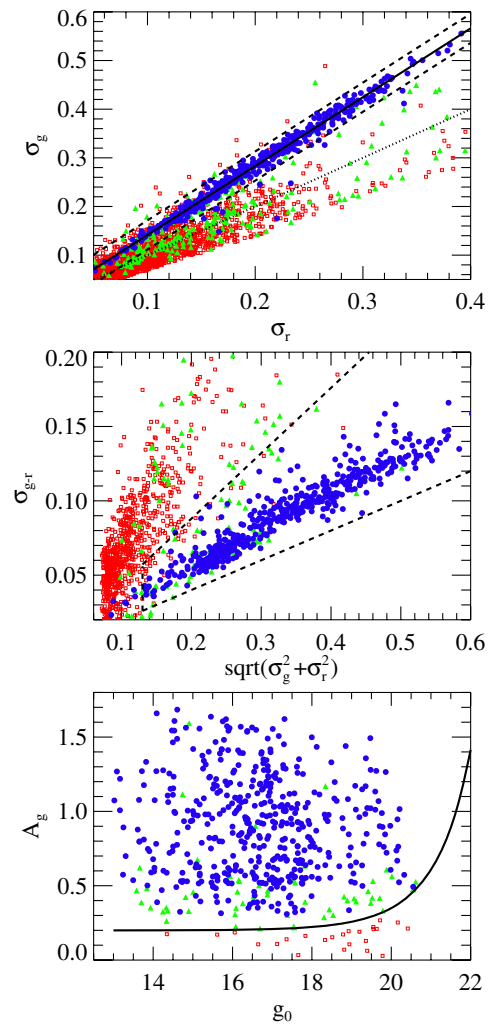


**Figure 3.** Top:  $\sigma_g$  vs.  $\sigma_r$  distribution of template-accepted (blue dots), template-rejected (red open squares), and ambiguous candidates (green triangles) before the  $|\sigma_g - 1.42\sigma_r| < 0.03$  selection (region between dashed lines). Note that the majority of template-rejected and ambiguous candidates do not follow the  $\sigma_g = 1.42\sigma_r$  relation typical of RR Lyrae stars (solid line), but rather the  $\sigma_g = \sigma_r$  relation (dotted line) that indicates non-pulsational variability. Middle:  $\sigma_{g-r}$  vs.  $\sqrt{(\sigma_g^2 + \sigma_r^2)}$  distribution of candidates from the top panel after the  $|\sigma_g - 1.42\sigma_r| < 0.03$  selection is applied. The dashed lines show the selection based on the  $\sigma_{g-r}$  and  $\sqrt{(\sigma_g^2 + \sigma_r^2)}$  values, where  $\sigma_{g-r}$  is the rms scatter in the  $g - r$  color. Bottom:  $A_g$  vs.  $\langle g \rangle$  distribution of candidates selected from the middle panel’s dashed box region. Note that almost all of the ambiguous candidates with  $g_0 \sim 20.5$  shown in Figure 2 are removed after top and middle panel cuts are made, while the template-accepted candidates remain.

(A color version of this figure is available in the online journal.)

region centered on the  $\sigma_g = 1.42\sigma_r$  (the rms scatter around  $\sigma_g = 1.42\sigma_r$  is 0.006 mag) line typical of RR Lyrae stars (Ivezić et al. 2000; S07), while the majority of template-rejected and ambiguous candidates follow the  $\sigma_g = \sigma_r$  relation that suggests non-pulsational variability. It is interesting to note that 13 template-accepted RR Lyrae stars have lower observed  $\sigma_g$  values (by  $>0.03$  mag) than what is predicted by the  $\sigma_g = 1.42\sigma_r$  ( $5\sigma$ ) relation. The  $g$ - and  $r$ -band light curves of two such stars are shown in Figure 4 (top and middle). Based on the Figure 3 (top) plot, we conclude that the majority of RR Lyrae stars (97%) have  $|\sigma_g - 1.42\sigma_r| < 0.03$ , and select all candidates that pass this condition for further analysis. The 13 template-accepted RR Lyrae stars found outside the  $|\sigma_g - 1.42\sigma_r| < 0.03$  region are also included as we believe they are RR Lyrae stars (based

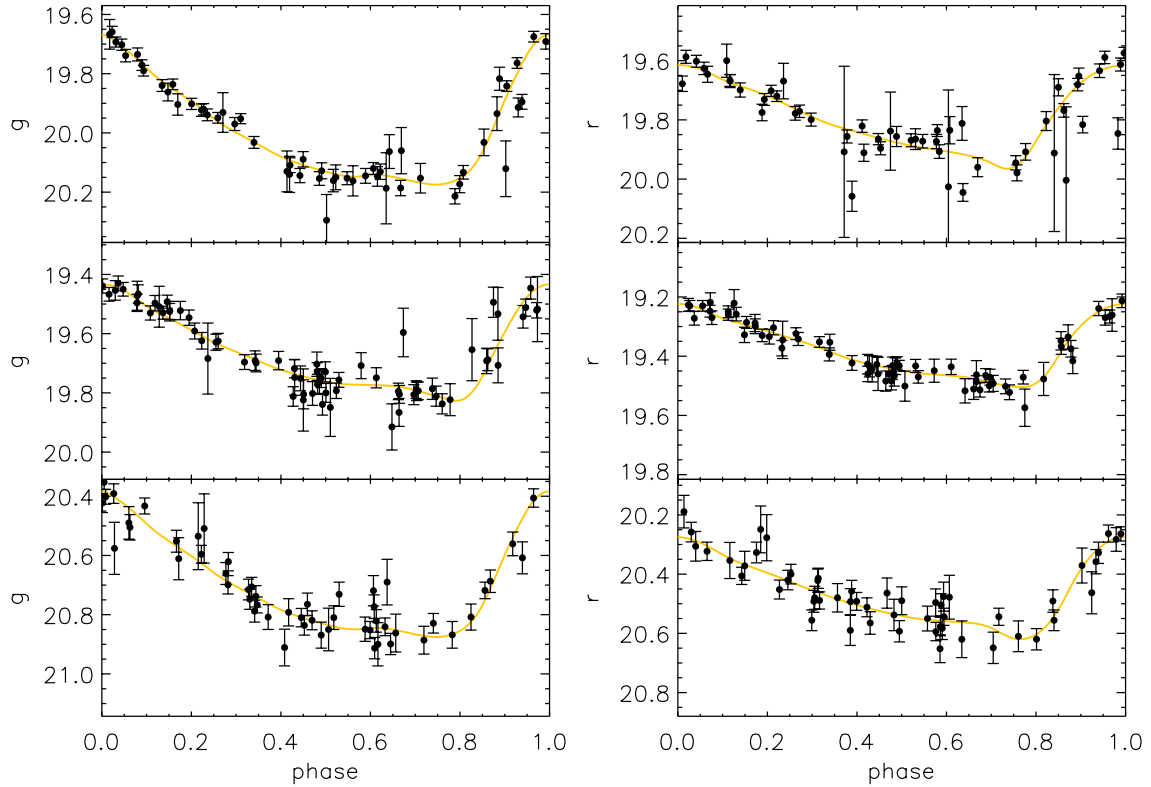


**Figure 4.** Top and middle panels show the  $g$ - (left) and  $r$ -band (right) light curves of two RR Lyrae stars with the observed  $\sigma_g$  slightly smaller than the predicted  $\sigma_g = 1.42\sigma_r$  value (by  $\sim 0.1$  mag). The bottom panel shows the  $g$ - and  $r$ -band light curves of an RR Lyrae star with  $\sigma_{g-r}$  greater by  $\sim 0.05$  mag than the cutoff dashed line in Figure 3 (bottom). The solid lines show the best-fit  $g$ - and  $r$ -band templates (see Section 3). All three stars have slightly peculiar  $\sigma_g$ ,  $\sigma_r$ , and  $\sigma_{g-r}$  values, but are still included in the final RR Lyrae sample as their light curves are very much RR Lyrae-like.

(A color version of this figure is available in the online journal.)

on their light curves), but with peculiar variability properties (slightly lower than expected rms scatter in the  $g$  band).

The candidates that pass the  $|\sigma_g - 1.42\sigma_r| < 0.03$  condition also separate well in the  $\sigma_{g-r}$  versus  $\sqrt{\sigma_g^2 + \sigma_r^2}$  plot (Figure 3, middle panel), which is sensitive to the covariance between the  $g$  and  $r$  bands. Using the distribution of template-accepted candidates as an indicator of where RR Lyrae stars exist in this plot, we make another selection and again plot the selected candidates in the  $g$ -band amplitude versus maximum brightness plot (Figure 3, bottom panel). There are eight template-accepted RR Lyrae stars that do not pass the  $\sigma_{g-r}$  versus  $\sqrt{\sigma_g^2 + \sigma_r^2}$  selection, one of which is shown in Figure 4 (bottom panel). As in the previous paragraph, we choose to keep these candidates as they might be RR Lyrae stars with peculiar variability properties (higher than expected rms scatter in the  $g-r$  color).

The utility of the  $\sigma_{g-r}$  selection is demonstrated in Figure 5, where we compare  $g$  and  $g-r$  light curves of a type  $c$  RR Lyrae (hereafter RRC) and a candidate eclipsing binary star. Even though their  $g$ -band light curves are quite similar and their periods match those of RRC stars, their  $g-r$  light curves are quite different. The  $g-r$  light curve of the eclipsing binary varies much less than that of the RRC star, as the binary is most probably comprised of two similar effective temperature stars. On the other hand, the effective temperature of the RRC star changes due to pulsations, and the variations in the  $g-r$  light curve are much greater.

A comparison of Figures 2 and 3 (bottom panel) shows that the majority of ambiguous and template-rejected candidates do not have variability properties ( $\sigma_g$ ,  $\sigma_r$ ,  $\sigma_{g-r}$ ) that are consistent

with variability properties of template-accepted RR Lyrae stars. Only 18% of ambiguous and 1% of template-rejected candidates pass our  $\sigma_g - \sigma_r - \sigma_{g-r}$  variability cuts, while only a small fraction of template-accepted candidates (4%) is rejected. Most importantly, almost all of the ambiguous candidates with  $g_0 \gtrsim 20.5$  were rejected based on their variability properties.

These results suggest that the candidates initially classified as template-accepted are indeed true RR Lyrae stars, but that some ambiguous and template-rejected candidates might also be true RR Lyrae stars. We have re-examined light curves of ambiguous and template-rejected candidates that pass the  $\sigma_g - \sigma_r - \sigma_{g-r}$  variability cuts, and re-classified four as template-accepted. The 21 template-accepted candidates that were slightly outside of our selection criteria were also kept, as the visual inspection of their  $g$  and  $g-r$  light curves strongly suggests they are indeed RR Lyrae stars. Finally, we report 483 stars in our SDSS stripe 82 RR Lyrae sample, and estimate it to be essentially complete and free of non-RR Lyrae stars.

Our high degree of completeness is achieved by relaxing color and variability cuts from S07, and by accepting stars that are slightly outside the selection region if their light curves are strongly RR Lyrae-like. We find that the median  $g-r$ ,  $r-i$ , and  $i-z$  colors of stars in the final sample are well within the ranges defined by Equations (2)–(4), and 20 of the selected stars ( $\sim 4\%$ ) have median  $u-g$  color in the  $0.85 < u-g < 0.98$  range. This finding validates the expansion of the  $u-g$  range blueward to 0.7 mag (from  $u-g = 0.98$  used in S07). The visual inspection of  $g$  and  $g-r$  light curves ensures that non-RR Lyrae stars are not included in the final sample.

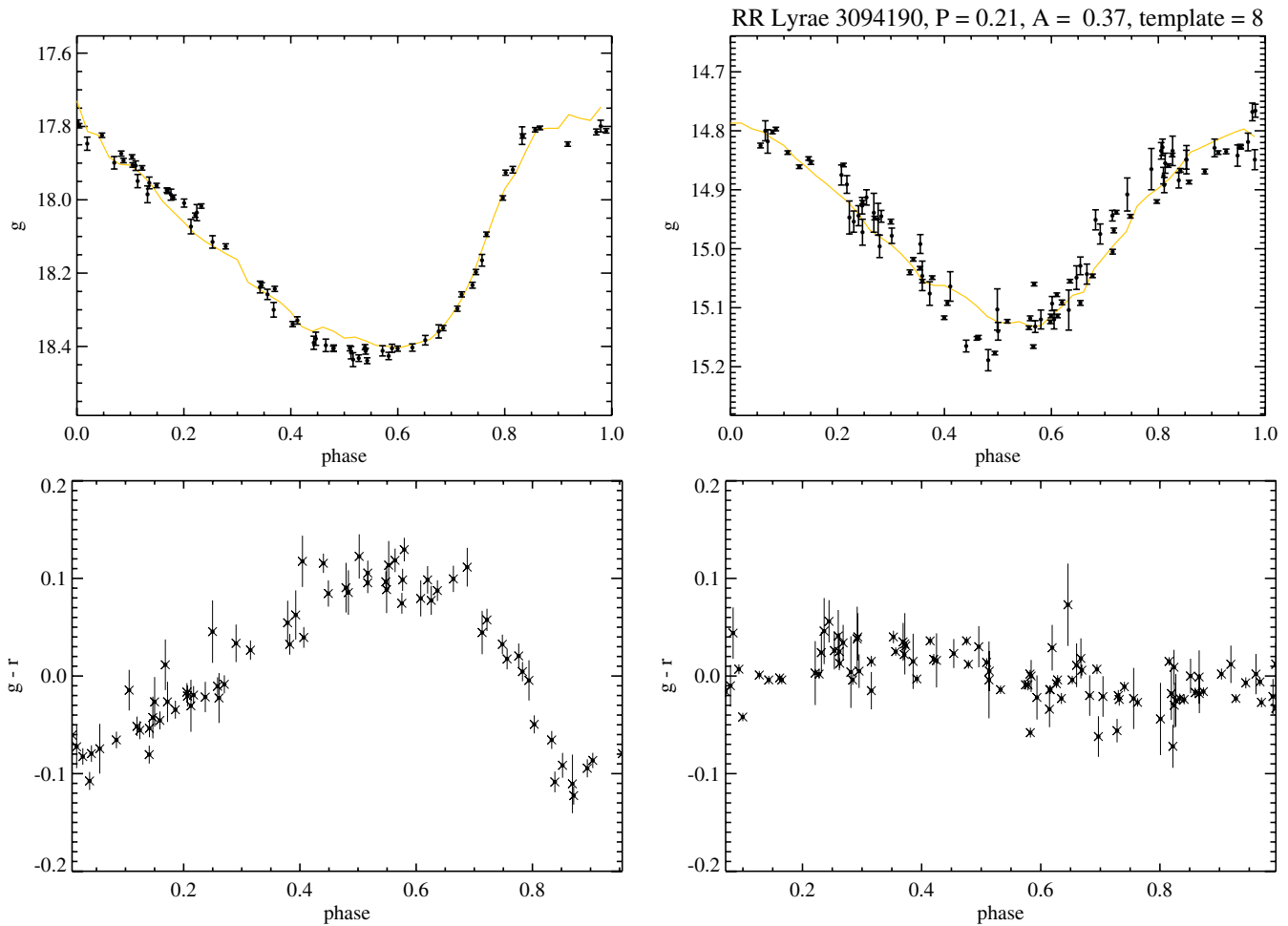


**Figure 5.**  $g$  (top) and  $g - r$  (bottom) light curves of an RRc star (left) and a candidate eclipsing binary (right). The best-fit  $V$ -band templates are shown as solid lines. Even though their  $g$ -band light curves are quite similar, and their periods are in the  $0.2 < P < 0.43$  days range typical of RRc stars, their  $g - r$  light curves are quite different. The eclipsing binary is outside the Figure 3 (middle) selection box as it has a much smaller rms scatter in the  $g - r$  color ( $\sigma_{g-r} \sim 0.02$  mag) than the RRc star ( $\sigma_{g-r} \sim 0.07$  mag).

(A color version of this figure is available in the online journal.)

When time-averaged colors are not available (as is the case for the majority of SDSS stars), a range of single-epoch colors might be more useful for the selection of RR Lyrae stars. We find that RR Lyrae stars have single-epoch colors in these ranges:

$$0.75 < u - g < 1.45, \quad (6)$$

$$-0.25 < g - r < 0.4, \quad (7)$$

$$-0.2 < r - i < 0.2, \quad (8)$$

$$-0.3 < i - z < 0.3. \quad (9)$$

### 3. THE $ugriz$ RR LYRAE TEMPLATES

The availability of a large sample of RR Lyrae stars with densely sampled light curves presents us with a unique opportunity to derive template RR Lyrae light curves for the SDSS photometric system. While template RR Lyrae light curves for the SDSS  $ugriz$  bands do exist in the literature (e.g., see Marconi et al. 2006), they are based on pulsation models, and not on actual observations. Recognizing the importance of such templates for future large sky surveys that will use the SDSS filter set, such as the Large Synoptic Survey Telescope (LSST; Ivezić et al. 2008) and Pan-STARRS (Kaiser et al. 2002), we now describe the construction of template  $ugriz$  RR Lyrae light curves.

#### 3.1. Construction of $ugriz$ RR Lyrae Templates

Our goal is to construct the smallest set of template  $ugriz$  RR Lyrae light curves that will model the light curves present in our sample at a level of uncertainty set by photometric errors ( $\sim 0.02$  mag). To achieve this goal, we use an iterative approach to refine the initial set of prototype templates.

First, for each  $ugriz$  band we find RR Lyrae stars that have at least 50 observations in a band with photometric errors less than 0.05 mag. The light curves of such RR Lyrae are period-folded, and a B-spline is interpolated through the data if the largest gap in the phase coverage is smaller than 0.05. The RR Lyrae stars with phase coverage gaps greater than 0.05 are not used in the construction of the RR Lyrae templates. The light curves with interpolated B-splines ( $\sim 100$  per band) are hereafter referred to as prototype templates, and are normalized to have values in the  $[0, 1]$  range and maxima at phase = 0.

In the next step, we fit the prototype templates to each of the 483 light curves and qualify a fit as acceptable if  $\zeta < 1.3$ . Here it is possible to have more than one acceptable template fit per light curve. The RR Lyrae stars with acceptable fits are grouped by prototype templates, and their observed light curves are period-folded and normalized using best-fit period, amplitude, mean magnitude, and epoch of the maximum brightness. The normalized light curves are grouped on a per template basis, and

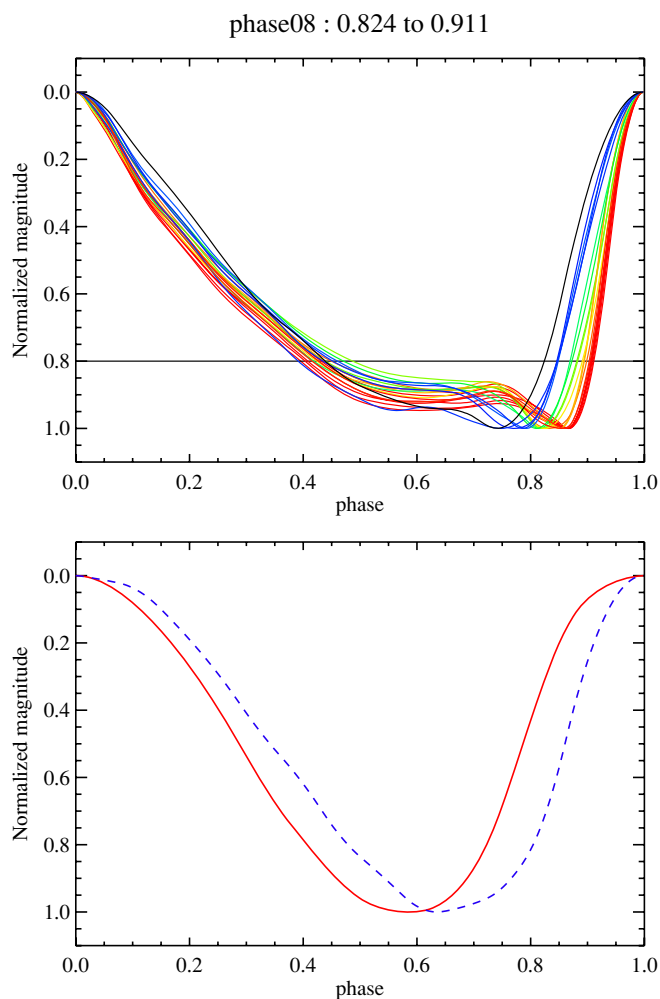


**Figure 6.** Top: 22  $g$ -band RR  $ab$ -type template light curves, color-coded from black to red using  $\phi_{0.8}^g$ , defined as the phase at which a  $g$ -band template value is equal to 0.8. The  $\phi_{0.8}$  is similar in principle to the rise time used by Sandage et al. (1981) and Layden (1998) (shorter rise time means higher  $\phi_{0.8}$ ). Bottom: a comparison of two  $g$ -band RR  $c$ -type template light curves. The template showed by the dashed line has a higher  $\phi_{0.8}^g$  value than the template showed by the solid line (0.80 vs. 0.72).

(A color version of this figure is available in the online journal.)

a B-spline is interpolated through the grouped data. With this procedure we smooth out prototype templates by averaging over similarly shaped light curves. In other words, the main purpose of the prototype templates is to select self-similar subsets of observed light curves.

Since the number of smoothed prototype templates is about 100 per band, it is possible that some of them are redundant and that they may be replaced by a single template without decreasing the generality of the template set. To establish which templates are redundant, we fit smoothed templates to RR Lyrae light curves and accept template fits with  $\zeta < 1.3$ . Again, it is possible to have more than one acceptable template fit per light curve.

We rank the smoothed templates by the number of light curves they fit, and sort them in descending order (the highest ranking template fits the greatest number of light curves). Starting with the second-ranked template, we count the number of light curves that were *not* fitted by the highest ranking template. We move down the template list and for each template count only light curves that were not already fitted by all higher ranking

templates. We stop moving down the template list when we reach a template that fits only one light curve.

The templates that survive this pruning are compared with each other, and if there are two with maximum difference less than 0.02 (the average photometric error), we keep the one that fits a greater number of light curves. Our final, pruned template set contains 12  $u$ -band (one is type  $c$ ), 23  $g$ -band (two are type  $c$ ), 22  $r$ -band (two are type  $c$ ), 22  $i$ -band (two are type  $c$ ), and 19  $z$ -band templates (one is type  $c$ ). The templates are provided in the supplementary data available in the electronic edition of the journal. The light curve parameters of stripe 82 RR Lyrae stars obtained from best-fit  $ugriz$  templates are listed Table 2.

As illustrated in Figure 6, the set of  $\sim 20$   $ab$  templates per band appears consistent with a continuous distribution of light curve shapes. This essentially one-dimensional template family can be conveniently parameterized by the phase at which the normalized template (with unit amplitude) crosses the value of 0.8 on the rising part of light curve (hereafter  $\phi_{0.8}$ ). This parameter measures the rise time, as a fraction of the period, and is related to other parameterizations of the light curve shape, such as the coefficients of a Fourier expansion (see Section 4.7.2).

On the other hand,  $c$ -type RR Lyrae stars exhibit a strong bimodal distribution of light curve shapes in the  $gri$  bands, suggesting that this class may include two distinct subclasses, with each subclass having very small scatter of light curve shapes. This behavior is further discussed in Section 4.6.

We also note that our template set is not entirely complete, as illustrated in Figure 7. There are 15 examples of stars (3%) for which the current template does not describe their (unique) light curves at the level of the photometric uncertainty (0.02 mag).

### 3.2. A Comparison with Theoretical Template Light Curves

In Figure 8, we compare empirical RRab templates to theoretical templates from Marconi et al. (2006). As the bandpass moves to longer wavelengths (from the  $g$  to  $z$  band), the light curve shape of both empirical and theoretical templates becomes less convex (less curved upward) on the descending brightness branch (phase  $< 0.7$ ). The light curve shape does not change significantly between  $u$  and  $g$  bands in neither empirical or theoretical templates.

On the other hand, the theoretical templates have a peak after the minimum brightness that is not observed in our templates. The differences between our empirical templates and theoretical templates are much larger than the errors in our templates. The new pulsation models will undoubtedly benefit from constraints provided by the observational template set derived here. Additional constraints may also be obtained from comparisons of theoretical (Figure 7 in Marconi et al. 2006) and observed color-color loops (Figure 9 in this work).

## 4. OUTER HALO SUBSTRUCTURE AS TRACED BY STRIPE 82 RR LYRAE STARS

In this section, the spatial distribution of RR Lyrae stars is used to trace the substructures in the outer halo. First, we estimate the heliocentric distances of RR Lyrae stars using their best-fit  $g$ - and  $r$ -band light curves, then estimate the sample completeness as a function of magnitude in Section 4.2. The observed spatial distribution of RR Lyrae stars is used to compute their number density distribution, which is then compared to a model number density distribution. This comparison reveals an abrupt change in the number density distribution at a distance

**Table 2**  
Light Curve Parameters for Stripe 82 RR Lyrae Stars

RR Lyrae <sup>a</sup>	Type	Period <sup>b</sup>	$A_u^c$	$u_0^d$	$\phi_0^{u,e}$	$T_u^f$	$A_g^c$	$g_0^d$	$\phi_0^{g,e}$	$T_g^f$	$A_r^c$	$r_0^d$	$\phi_0^{r,e}$	$T_r^f$	$A_i^c$	$i_0^d$	$\phi_0^{i,e}$	$T_i^f$	$A_z^c$	$z_0^d$	$\phi_0^{z,e}$	$T_z^f$
4099	ab	0.642	0.53	17.82	51075.27	101	0.56	16.66	51075.28	101	0.40	16.56	51075.29	103	0.32	16.55	51075.29	102	0.30	16.54	51075.28	100
13350	ab	0.548	1.03	18.24	54025.33	107	1.09	16.99	54025.32	120	0.80	17.09	54025.32	112	0.64	17.15	54025.32	116	0.58	17.19	54025.32	114
15927	ab	0.612	0.65	18.92	53680.22	102	0.70	17.65	53680.22	106	0.49	17.60	53680.22	108	0.37	17.61	53680.24	104	0.35	17.62	53680.24	100
20406	ab	0.632	0.55	16.38	54000.28	100	0.59	15.21	54000.29	101	0.43	15.12	54000.27	108	0.34	15.12	54000.29	102	0.30	15.13	54000.29	100
21992	ab	0.626	1.11	15.53	53698.24	106	1.14	14.38	53698.24	112	0.85	14.42	53698.24	114	0.66	14.52	53698.24	111	0.62	14.52	53698.24	114

**Notes.**

<sup>a</sup> RR Lyrae ID number.

<sup>b</sup> Period in days.

<sup>c</sup> Amplitude determined from the best-fit template.

<sup>d</sup> Mean magnitude corrected for the ISM extinction and determined from the best-fit template.

<sup>e</sup> Epoch of maximum brightness determined from the best-fit template.

<sup>f</sup> Best-fit template ID number.

(This table is available in its entirety in a machine-readable form in the online journal. A portion is shown here for guidance regarding its form and content.)

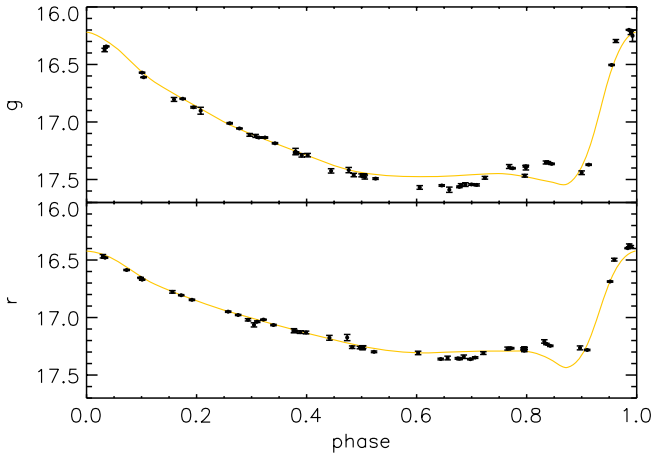


**Figure 7.** Example of incompleteness in our RR Lyrae light curve template set. The period-folded  $g$ - and  $r$ -band light curves are shown with symbols, and the best-fit templates are shown with solid lines. The fact that even the best-fit templates fail to model these light curves at minimum brightness ( $0.5 < \text{phase} < 0.9$ ) suggests that our light curve template set is not entirely complete.

(A color version of this figure is available in the online journal.)

of  $\sim 30$  kpc, suggesting a transition from the inner to outer halo, as well as the presence of a prominent halo overdensity at 80 kpc.

#### 4.1. Distance Estimates

The heliocentric distances,  $d$ , for RR Lyrae stars are estimated from measurements of their mean dereddened  $V$  magnitudes,  $\langle V \rangle$ , and by assuming an average value for their absolute magnitudes,  $M_V$

$$d = 10^{(\langle V \rangle - M_V + 5)/5}. \quad (10)$$

For the absolute magnitude in the  $V$  band we adopt  $M_V = 0.6$ , calculated using the Cacciari & Clementini (2003)  $M_V - [\text{Fe}/\text{H}]$  relation

$$M_V = (0.23 \pm 0.04)[\text{Fe}/\text{H}] + (0.93 \pm 0.12) \quad (11)$$

and adopting  $[\text{Fe}/\text{H}] = -1.5$  as the mean halo metallicity (Ivezić et al. 2008).

The values of  $\langle V \rangle$  are determined by integrating best-fit template  $V$ -band light curves after transformation to flux units. The best-fit template  $V$ -band light curves are synthesized from the best-fit  $g$ - and  $r$ -band templates ( $g_{\text{LC}}(\phi)$  and  $r_{\text{LC}}(\phi)$ ) using a photometric transformation given by Equation (10) from Ivezić et al. (2007),

$$gr_{\text{LC}}(\phi) = g_{\text{LC}}(\phi) - r_{\text{LC}}(\phi), \quad (12)$$

$$V_{\text{LC}}(\phi) = g_{\text{LC}}(\phi) + 0.0688gr_{\text{LC}}(\phi)^3 - 0.2056gr_{\text{LC}}(\phi)^2 - 0.3838gr_{\text{LC}}(\phi) - 0.053, \quad (13)$$

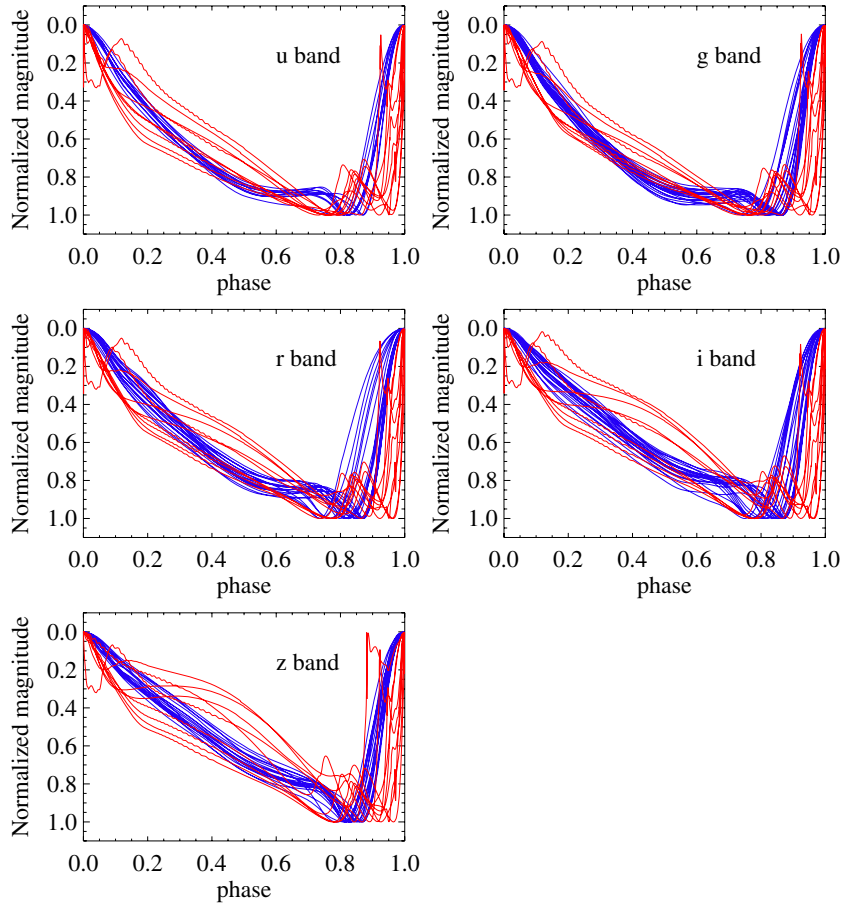


**Figure 8.** Comparison of empirical (blue lines) and theoretical (red lines) RR  $ab$ -type template light curves in SDSS  $ugriz$  bandpasses. The theoretical Marconi et al. (2006) templates were obtained from an RR Lyrae pulsational model with metallicity  $Z = 0.001$ , luminosity  $L = 1.61 L_{\odot}$ , mass  $M = 0.75 M_{\odot}$ , and effective temperature  $T_{\text{eff}} = 6100\text{--}6900$  K. Note how the light curve shape of empirical and theoretical templates changes significantly between  $griz$  bands, becoming less convex (less curved upward) on the descending brightness branch (phase  $< 0.7$ ) as the bandpass moves to longer wavelengths. The shape does not change significantly between  $u$  and  $g$  bands.

(A color version of this figure is available in the online journal.)

**Table 3**  
Positions and Derived Parameters of Stripe 82 RR Lyrae Stars

RR Lyrae <sup>a</sup>	R.A. <sup>b</sup>	Decl. <sup>b</sup>	rExt <sup>c</sup>	$d^d$	$R_{GC}^d$	$\langle u \rangle^e$	$\langle g \rangle^e$	$\langle r \rangle^e$	$\langle i \rangle^e$	$\langle z \rangle^e$	$\langle V \rangle^e$	$\langle u - g \rangle_{\min}^f$	$\sigma_{\langle u - g \rangle_{\min}}^f$	$\langle g - r \rangle_{\min}^g$	$\sigma_{\langle g - r \rangle_{\min}}^g$
4099	0.935679	1.115859	0.089	17.75	20.03	18.13	16.99	16.78	16.70	16.68	16.85	1.10	0.02	0.28	0.01
13350	0.283437	1.178522	0.080	24.77	26.55	18.84	17.68	17.54	17.50	17.50	17.57	1.16	0.01	0.26	0.01
15927	3.254658	-0.584066	0.090	29.12	30.96	19.29	18.06	17.86	17.79	17.78	17.92	1.24	0.02	0.28	0.01
20406	3.244369	0.218891	0.088	9.13	12.76	16.71	15.54	15.34	15.29	15.28	15.40	1.18	0.01	0.27	0.01
21992	4.315354	1.054582	0.077	7.35	11.54	16.19	15.04	14.91	14.86	14.85	14.93	1.13	0.01	0.25	0.01

**Notes.**

<sup>a</sup> RR Lyrae ID number.

<sup>b</sup> Median equatorial J2000.0 right ascension and declination in degrees.

<sup>c</sup> ISM extinction in the SDSS  $r$  band obtained from Schlegel et al. (1998).

<sup>d</sup> Heliocentric and galactocentric distance in kpc.

<sup>e</sup> Flux-averaged magnitudes corrected for ISM extinction.

<sup>f</sup> Median  $u - g$  color (corrected for ISM extinction) at the minimum brightness and the uncertainty in the median.

<sup>g</sup> Median  $g - r$  color (corrected for ISM extinction) at the minimum brightness and the uncertainty in the median.

(This table is available in its entirety in a machine-readable form in the online journal. A portion is shown here for guidance regarding its form and content.)

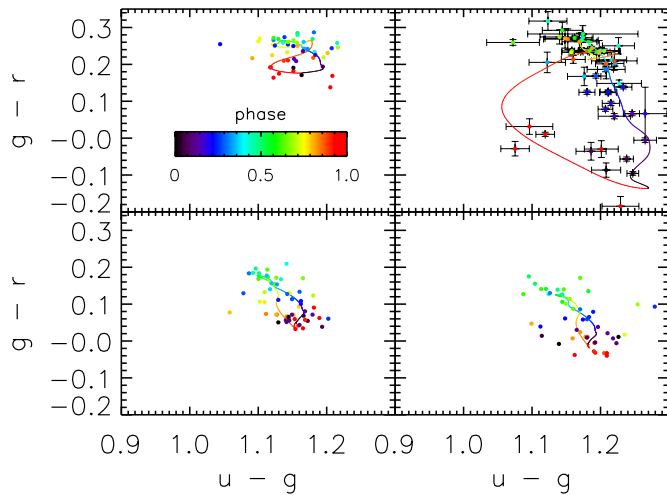


**Figure 9.**  $u - g$  vs.  $g - r$  color-color loops of four RR Lyrae stars. The top left panel shows a long-period, low-amplitude type  $b$  RR Lyrae stars (ID 276162), the top right panel shows a short-period, large-amplitude type  $a$  RR Lyrae star (ID 293282), and the bottom panels show two type  $c$  RR Lyrae stars (IDs 376465 and 429508), with the one on the left having a longer period and a lower amplitude than the one on the right. The observed (symbols with error bars) and predicted  $u - g$  and  $g - r$  colors (from the best-fit  $ugr$ -band templates, lines) are color-coded according to the phase of pulsation. The error bars are not shown in three panels to avoid cluttering. The amplitude in the  $g - r$  color increases with the  $g$ -band amplitude ( $A_{g-r} \sim 0.4A_g$ , since  $A_g \sim 1.4A_r$  and  $A_{g-r} \sim A_g - A_r$ ). The color-color loops for the rest of the RR Lyrae stars are provided in the electronic edition of the journal.

(The complete figure set (483 images) is available in the online journal.)

where  $\phi \in [0, 1)$  is the phase of pulsation, and where  $g_{LC}(\phi)$  and  $r_{LC}(\phi)$  are corrected for interstellar extinction. We have also established that the measured light curves are aligned in phase among the bands to within the measurement errors (to within 1% in phase). These “flux-averaged” magnitudes are used because pulsation models show that they better reproduce the behavior of “static” magnitudes (the magnitudes the stars would have if they were not pulsating; Marconi et al. 2006). The uncertainty in  $\langle V \rangle$  is mainly due to photometric errors in the  $g$  and  $r$  bands, and is estimated to be  $\sim 0.03$  mag.

Following the discussion by Vivas & Zinn (2006) (see their Section 4), we adopt  $\sigma_{M_V} = \sqrt{(\sigma_{M_V}^{[Fe/H]})^2 + (\Delta M_V^{ev})^2} = 0.1$  mag as the uncertainty in absolute magnitude, where  $\sigma_{M_V}^{[Fe/H]} =$

0.07 mag is the uncertainty due to metallicity dispersion ( $\sigma_{[Fe/H]} = 0.3$  dex; Ivezić et al. 2008), and  $\Delta M_V^{ev} = 0.08$  mag is the uncertainty due to RR Lyrae evolution off the zero-age horizontal branch (Vivas & Zinn 2006). The estimated fractional error in the heliocentric distance ( $d/\sigma_d$ ) of 0.06 is smaller, by a factor of  $\sim 2-4$ , than the fractional distance error for K giants (Dohm-Palmer et al. 2001), M giants (Majewski et al. 2003), or main-sequence stars (Newberg et al. 2002; Jurić et al. 2008). The heliocentric distances and equatorial coordinates of stripe 82 RR Lyrae stars are listed in Table 3.

#### 4.2. Sample Completeness as a Function of Magnitude

The fraction of recovered RR Lyrae stars (the completeness) as a function of apparent magnitude is an important question that needs to be considered before the spatial distribution of RR Lyrae stars can be discussed. We generate 1000 RRAb synthetic  $g$ -band light curves with 30 data points, amplitudes of 1.0 mag, periods of 0.6 days, and with flux-averaged magnitudes of  $\langle g \rangle = 21.6$  (not corrected for ISM extinction). An RR Lyrae star with  $\langle g \rangle = 21.6$  would be located at  $\sim 120$  kpc, assuming  $M_g = 0.6$  and 0.6 mag of ISM extinction in the  $g$  band (the highest observed extinction in stripe 82). Typical random photometric errors were added as a function of magnitude using Figure 1 from S07. The periods for the synthetic light curves were estimated using *Supersmoother*, and the amplitudes and maximum brightness were estimated from best-fit templates.

We find that the periods are recovered with 0.05% (or better) accuracy, and flux-averaged magnitudes with 0.03 mag (or better) accuracy. Similar results are obtained for RRC stars (the amplitude of synthetic light curve is 0.5 mag in that case). If we define an RR Lyrae as successfully recovered if its flux-averaged magnitude is estimated with 0.03 mag accuracy, then the stripe 82 RR Lyrae sample is essentially 100% complete to 120 kpc, even in regions where the extinction is as high as 0.6 mag ( $R.A. > 50^\circ$  and  $R.A. < 308^\circ$ ).

Even though both RRAb and RRC types have the same completeness as a function of apparent magnitude, we only use RRAb types when studying the spatial distribution of RR Lyrae stars, because they represent a homogeneous and robust sample with a well-studied absolute magnitude versus metallicity distribution. A repeat of the analysis presented below, but with RRC stars included, did not change our conclusions based exclusively on RRAb stars.

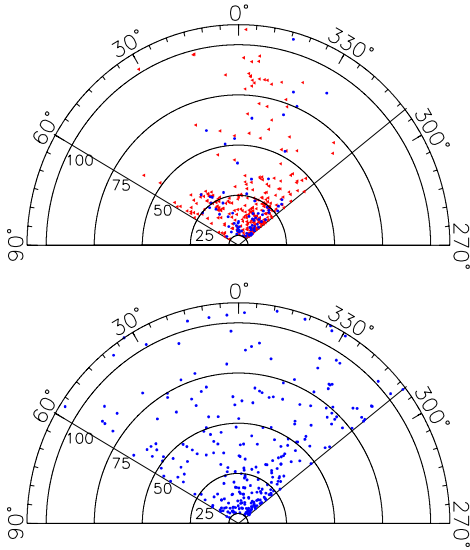


**Figure 10.** Top panel shows the spatial distribution of 366 RRab stars from stripe 82, while the bottom panel shows 302 stars randomly drawn from a smooth model distribution (Equation (16)). Both samples of stars have heliocentric distances between 5 and 120 kpc and  $|\text{decl.}| < 1^\circ 25'$ . The radial axis is the heliocentric distance in kpc and the angle is the equatorial right ascension. The circles correspond to  $\langle V \rangle$  of 16.3, 17.8, 18.7, and 19.3 mag (corrected for ISM extinction). The RRab stars shown in the top panel are divided into Oosterhoff I (289 stars, red triangles) and Oosterhoff II (77 stars, blue dots) using the selection boundary shown in Figure 16.

(A color version of this figure is available in the online journal.)

#### 4.3. Observed Spatial Distribution

Since SDSS stripe 82 is quite narrow in declination ( $2^\circ 5'$  compared to  $118^\circ$  in R.A.), we assume  $\text{decl.} = 0$  for all stars, and describe their positions in the R.A.–heliocentric distance space. The Cartesian coordinates of stars in this space are defined as

$$x = d \cos(\alpha), \quad (14)$$

$$y = d \sin(\alpha), \quad (15)$$

where  $d$  is the heliocentric distance in kpc and  $\alpha$  is the right ascension angle.

The spatial distribution of 366 RRab stars in the R.A.–heliocentric distance space is shown in Figure 10. For comparison, we also show the distribution of RR Lyrae stars randomly drawn from a smooth model number density distribution, based on an analysis of main-sequence stars within 20 kpc by Jurić et al. (2008)

$$\rho_{\text{model}}^{\text{RR}}(R, Z) = \rho_{\odot}^{\text{RR}} \left[ \frac{R_{\odot}}{\sqrt{R^2 + (Z/q_H)^2}} \right]^{n_H}, \quad (16)$$

where  $\rho_{\odot}^{\text{RR}} = 4.2 \text{ kpc}^{-3}$  is the number density of RRab stars at  $R_{\odot} = 8.0 \text{ kpc}$  (Vivas & Zinn 2006),  $q_H = 0.64$  indicates the halo is oblate (“squashed” in the same sense as the disk), and  $n_H = 2.77$  is the power-law index (Jurić et al. 2008). The expected number of RR Lyrae stars (according to  $\rho_{\text{model}}^{\text{RR}}$ ) in the 5–120 kpc range of stripe 82 is 302. The value of  $\rho_{\odot}^{\text{RR}}$  is within  $\pm 0.5 \text{ kpc}^{-3}$  from values reported by other authors (Preston et al. 1991; Suntzeff et al. 1991; Wetterer & McGraw 1996), and the uncertainty in  $n_H$  and  $q_H$  is  $\lesssim 0.2$  (Jurić et al. 2008). We also repeated the following analysis using a spherical,  $1/R^3$

halo model and obtained similar results and conclusions (i.e., detection of significant overdensities and the steepening of the halo density profile).

The two distributions shown in Figure 10 appear remarkably different. The observed distribution, shown in the top panel, has two overdense regions within 30 kpc; the one at R.A.  $\sim 30^\circ$  can be identified as the trailing arm of the Sagittarius dwarf spheroidal (dSph) tidal stream (Ivezić et al. 2003), while the other at R.A.  $\sim 330^\circ$  is likely associated with the Hercules–Aquila Cloud (Belokurov et al. 2007b). Beyond 30 kpc, the observed distribution is quite inhomogeneous in the R.A. direction, with the majority of RR Lyrae in the  $330^\circ$  to  $0^\circ$  region, and only a few RR Lyrae outside of it. On the other hand, the distribution of stars generated using Equation (16) looks more homogeneous, as expected.

#### 4.4. Bayesian Number Density Maps

We compute the local number density of RR Lyrae stars using a Bayesian estimator developed by Ivezić et al. (2005, see their Appendix B2 and Equation (B6)). The Bayesian metric presented there can be recast in a much simpler form

$$\rho_{\text{Bayes}} = C \frac{N_{nn}^k}{N_{\text{stars}} \sum_{i=1}^{N_{nn}} r_i^k}, \quad (17)$$

where  $N_{nn}$  is the number of nearest neighbors to which the distance  $r$  in a  $k$ -dimensional space is calculated, and  $N_{\text{stars}}$  is the number of stars. The dimensionless constant  $C$  involves complex integrals, but can be easily determined empirically once the geometry of the space in which densities need to be calculated is known.

To estimate the constant  $C$  we use the following procedure. We populate the stripe 82 region with  $N_{\text{stars}} = 302$  stars randomly drawn from the smooth model number density distribution (Equation (16)), and calculate the Bayesian metric on a  $0.5 \times 0.5 \text{ x } -y$  grid assuming  $N_{nn} = 8$ ,  $k = 2$ , and  $C = 1$ . The nearest neighbors are found using an implementation of the nearest neighbor searching algorithm (Arya et al. 1998). The number density is then calculated as

$$\rho(x, y) = \rho_{\text{Bayes}}(x, y)/d(x, y), \quad (18)$$

where the Bayesian metric is divided by the heliocentric distance to account for the increase in volume of a grid point at greater heliocentric distances. We generate 1000  $\rho(x, y)$  density maps, and average them out to obtain  $\rho_{\text{avg}}(x, y) = \sum \rho(x, y)/1000$ . The constant  $C = 1030$  is estimated by requiring the median value of  $\rho_{\text{avg}}(x, y)$  to equal the median value of  $\rho_{\text{model}}^{\text{RR}}(x, y)$ .

The sparseness of our sample (366 RR Lyrae in a volume of  $38,000 \text{ kpc}^3$ ) will result in random (Poisson) number density fluctuations even for a smooth underlying density distribution. To quantify the scatter in number density maps and to estimate the fraction of highly overdense and underdense pixels ( $|\log(\rho/\rho_{\text{model}}^{\text{RR}})| > 1$ ) due to Poisson fluctuations, we generate 1000 random RR Lyrae star samples of the same size as the observed sample by drawing them from the smooth model, and compute  $\log(\rho/\rho_{\text{model}}^{\text{RR}})$  maps for each sample. We find that the median rms scatter in smooth model-based maps is 0.3 dex (or about a factor of 2 on the linear scale), and that the fraction of highly overdense and underdense pixels ( $|\log(\rho/\rho_{\text{model}}^{\text{RR}})| > 1$ ) is only  $10^{-6}$ . We conclude that the precision of the Bayesian density estimator, given the sparseness of our sample, is about 0.3 dex, and that highly overdense and underdense pixels are not likely to be caused by Poisson fluctuations.

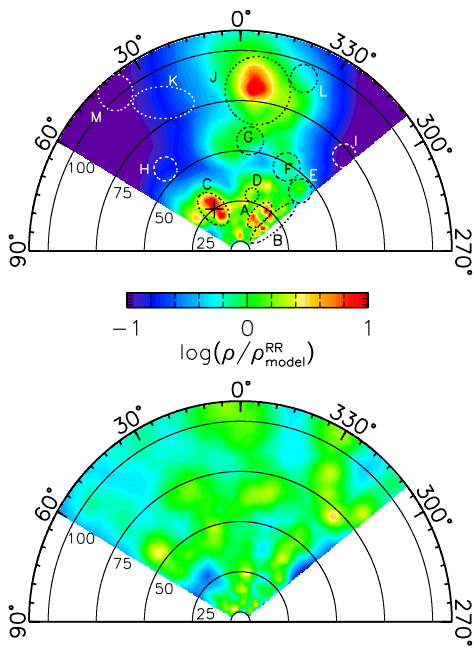


**Figure 11.** Number density distribution of observed (top) and smooth model-based (bottom) RR Lyrae stars from Figure 10, computed using Equation (18), and shown relative to the smooth model number density ( $\rho_{\text{model}}^{\text{RR}}$ ). The  $\log(\rho/\rho_{\text{model}}^{\text{RR}})$  values are color-coded according to the legend, with values outside the legend’s range saturating in purple and red, respectively. The stripe 82 plane intersects the Sagittarius dSph tidal stream (trailing arm) at ( $\sim 25$  kpc,  $\sim 30^\circ$ ), the Hercules–Aquila cloud at ( $\lesssim 25$  kpc,  $\sim 330^\circ$ ), and the Pisces stream at ( $\sim 80$  kpc,  $\sim 355^\circ$ ). The overdensities detected in S07 are overplotted and labeled in the top panel. The “+” symbol marks the position where the Law et al. (2005) “spherical” model of the Sagittarius dSph tidal stream (trailing arm) intersects the stripe 82 plane.

With the Bayesian density estimator now fully defined, we compute the number density  $\rho(x, y)$  on a  $x$ – $y$  grid for the observed distribution of RR Lyrae stars and for the sample of stars randomly drawn from the smooth model distribution. The computed number density maps are divided by  $\rho_{\text{model}}^{\text{RR}}(x, y)$ ; the results are shown in Figure 11.

Figure 11 (top) vividly shows the striking difference between the observed number density distribution of RR Lyrae stars and the smooth model number density distribution (Equation (16)). While the density fluctuations ( $\log(\rho/\rho_{\text{model}}^{\text{RR}})$ ) in the model-based map (Figure 11 [bottom]) are consistent with Poisson noise (amplitudes are  $< 0.3$  dex), the observed (top) map has several overdense and underdense regions (by a factor of 10 or more relative to  $\rho_{\text{model}}^{\text{RR}}$ ). The Sagittarius dSph tidal stream (trailing arm) is visible at  $\sim 25$  kpc and  $30^\circ$ , the Hercules–Aquila cloud is located at  $\lesssim 25$  kpc and  $\sim 330^\circ$ , and a previously detected, and now confirmed, structure can be seen at  $\sim 80$  kpc and  $\sim 355^\circ$  (the “J” overdensity in S07 Figure 13). The fraction of pixels with  $|\log(\rho/\rho_{\text{model}}^{\text{RR}})| > 1$  in the observed number density map is about 0.3 (dominated by underdense pixels), or 5 orders of magnitude higher than expected for Poisson fluctuations.

Figure 11 (top) also shows that some overdensities detected by S07 are not reproduced in this work. These overdensities were caused by non-RR Lyrae stars in the S07 candidate RR Lyrae sample (Table 4 lists the number of RR Lyrae and non-RR Lyrae stars in each S07 overdensity). About 70% of S07 RR Lyrae candidates are true RR Lyrae stars, with the reclassified non-RR Lyrae stars dominated by  $\delta$  Scuti stars (based on their light curves and periods). These results are in good

**Table 4**  
Sesar et al. (2007) Overdensities Revisited

S07 Label <sup>a</sup>	$N_{\text{tot}}$ <sup>b</sup>	$N_{\text{RRLyrae}}$ <sup>c</sup>	$N_{\text{non-RRLyrae}}$ <sup>d</sup>	$N_{\text{non-var}}$ <sup>e</sup>	$N_{\text{RRLyrae}}/N_{\text{tot}}$ <sup>f</sup>
A	84	76	7	1	0.91
B	144	98	44	2	0.68
C	54	50	4	0	0.93
D	8	5	3	0	0.63
E	11	7	4	0	0.64
F	11	4	7	0	0.36
G	10	5	5	0	0.50
H	7	0	7	0	0.00
I	4	1	3	0	0.25
J	26	12	14	0	0.46
K	8	1	7	0	0.13
L	3	0	3	0	0.00
M	5	1	4	0	0.20
All	375	260	112	3	0.69

**Notes.**

- <sup>a</sup> Overdensity label from S07.
- <sup>b</sup> Number of S07 candidate RR Lyrae in the overdensity.
- <sup>c</sup> Number of true RR Lyrae stars.
- <sup>d</sup> Number of variable, non-RR Lyrae stars.
- <sup>e</sup> Number of non-variable stars.
- <sup>f</sup> Fraction of true RR Lyrae stars.

agreement with S07 estimates. The overdensities labeled D, F, H, I, K, and L now have lower numbers of true RR Lyrae stars compared to S07, and are no longer significant overdensities. These overdensities were also speculated in S07 to be false detections. The significance of the E, G, and M overdensities decreased as the number of true RR Lyrae stars decreased compared to S07, and no longer seem to be real substructures.

The extension of the J overdensity in S07 in the radial direction due to the uncertainty in distance (the “finger of God” effect) is now smaller than in S07. In S07, the apparent  $V$ -band magnitudes of RR Lyrae stars were computed using Equation (3) from Ivezić et al. (2005) and using single-epoch measurements:

$$V_{\text{SDSS}}^{\text{RRLyrae}} = r - 2.06(g - r) + 0.355. \quad (19)$$

While this approximation works fairly well for RRab stars (the rms scatter around the fit is  $\sim 0.1$  mag), it produces an offset of  $\sim 0.3$  mag when applied to RRc stars, due to a 0.1 mag offset in their  $g - r$  colors (RRc stars have bluer  $g - r$  colors than RRab stars). The higher fraction of RRab than RRc stars in the Ivezić et al. (2005) RR Lyrae sample may explain the resulting bias in Equation (19) (Ivezić et al. 2005 did not fit Equation (19) separately for RRab and RRc stars). In this work, we use flux-averaged  $V$ -band apparent magnitudes and obtain more precise distance estimates for both RRab and RRc stars.

The structure at  $\sim 80$  kpc and  $\sim 355^\circ$  (labeled J in S07) is most probably a tidal stream, although the possibility that it is a dSph satellite galaxy cannot be excluded with the data presented here. It is unlikely that this structure is associated with the Sagittarius dSph stream because it is  $\sim 22$  kpc away from the best-fit orbital plane defined by Majewski et al. (2003). For comparison, the Sgr dSph trailing tidal stream and the stream detected by Newberg et al. (2003) are both within 2 kpc of the Sgr dSph plane. Watkins et al. (2009) point out that the location of the J overdensity is close to the Magellanic Plane, though at a larger galactocentric distance than the clouds. They also proposed to name the J overdensity as “the Pisces overdensity,” following the tradition of naming stellar streams and structures according to the nearest constellation. We adopt their proposal hereafter.

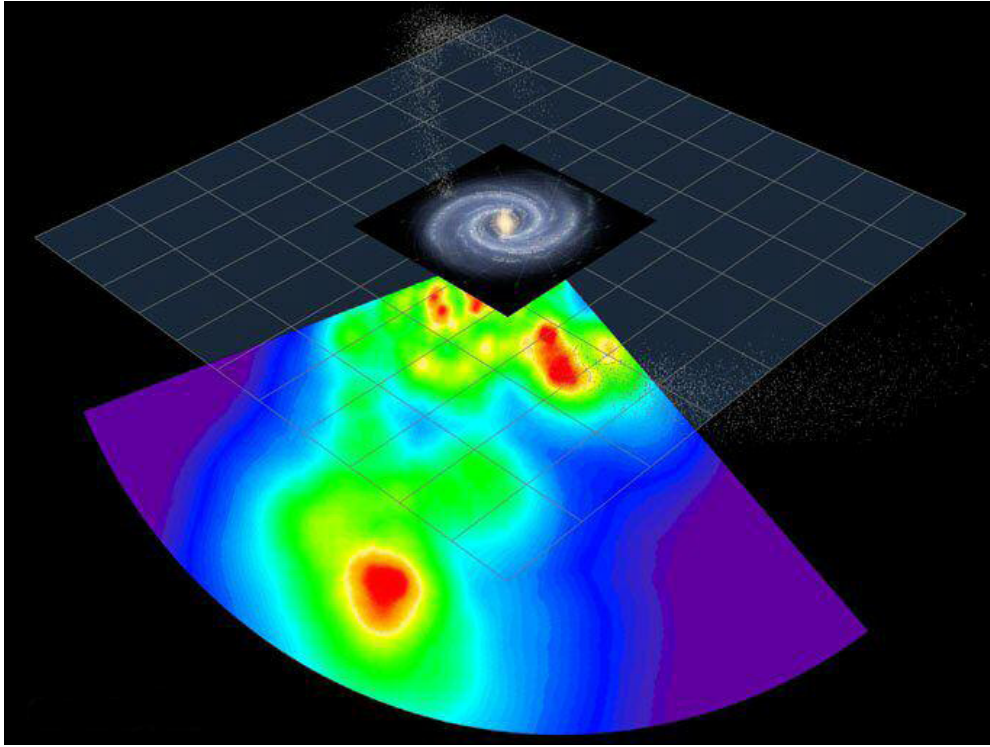


**Figure 12.** Single frame of an animation showing a fly-by of the stripe 82 plane and of the scaled Galactic plane (annotated artist’s concept by NASA/JPL-Caltech). The white dots show the Sagittarius dSph and its tidal streams, as modeled by the Law et al. (2005) “spherical” model. (An animation of this figure is available in the online journal.)

The width of the Pisces overdensity/stream in the radial direction ( $\sim 4$  kpc) is consistent with the scatter due to uncertainty in distance, while the scatter in the R.A. direction ( $\sim 4$  kpc) might be a projection effect (a combination of the stream’s incidence angle and thickness of the stripe 82 plane), or evidence of the stream’s width in the R.A. direction. To illustrate the scale and position of this and other detected structures, we provide an animation showing a “fly-by” of the stripe 82 region. The animation is provided in the electronic edition of the journal; a single frame is shown as Figure 12.

#### 4.5. The Steepening of the Halo Density Profile

The observed number density map (Figure 11 top panel) suggests that the smooth model (Equation (16)) systematically overestimates the observed number densities at galactocentric distances  $R_{GC} > 30$  kpc. We investigate this discrepancy in Figure 13 (top) by comparing the observed  $\log(\rho/\rho_{model}^{RR})$  distributions within  $R_{GC} < 30$  and  $R_{GC} < 110$  kpc with the distribution obtained from model-based number density maps. After a 33% increase in the model normalization ( $\rho_{\odot}^{RR}$  from Equation (16)), the observed and model-based distributions match well for  $R_{GC} < 30$  kpc. About 80% of the halo volume within  $R_{GC} < 30$  kpc is consistent with the smooth model (within Poisson noise limits,  $|\log(\rho/\rho_{model}^{RR})| < 0.3$ ); about 20% of the halo volume is found in predominantly overdense, substructures. The overdense tail of the distribution is more pronounced beyond 30 kpc. At these larger radii, the cumulative distribution (Figure 13 [bottom]) indicates that most of the probed halo volume is underdense, relative to the adopted smooth model (which is extrapolated from observations of main-sequence stars within  $\sim 20$  kpc).

The apparent need for a steeper density power-law index at  $R_{GC} > 30$  kpc is also illustrated in Figure 14, where we

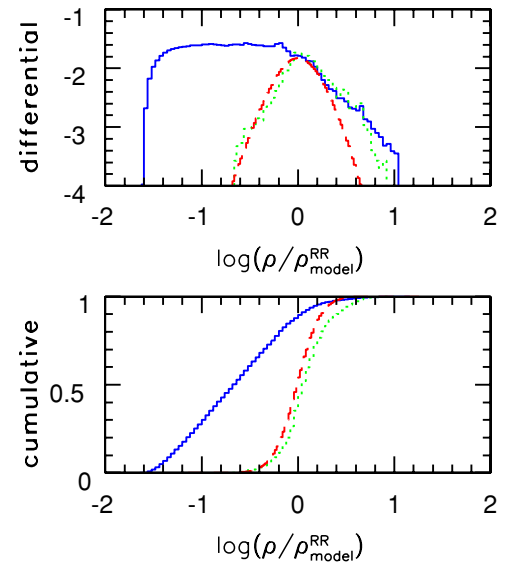


**Figure 13.** Differential (top, log y-axis) and cumulative (bottom) distribution of  $\log(\rho/\rho_{model}^{RR})$  in model-based (dashed line) and observed number density maps (solid line, within 110 kpc; dotted line, within 30 kpc). The slope of the observed  $\log(\rho/\rho_{model}^{RR})$  distribution in the  $0.3 < \log(\rho/\rho_{model}^{RR}) < 1.0$  range is  $-1.65 \pm 0.05$  within 110 kpc, and  $-1.91 \pm 0.09$  within 30 kpc. Note significantly higher fractions of strongly overdense and underdense regions than predicted by a smooth halo model.

plot the number density of RR Lyrae stars as a function of position angle and galactocentric distance. For  $R_{GC} > 30$  kpc and directions that avoid the Pisces overdensity, the Watkins et al. (2009) best-fit “broken” power-law (based on essentially the same RR Lyrae sample) provides a good fit with a  $n_H = 4.5$  power-law slope (apart from normalization: we had to scale

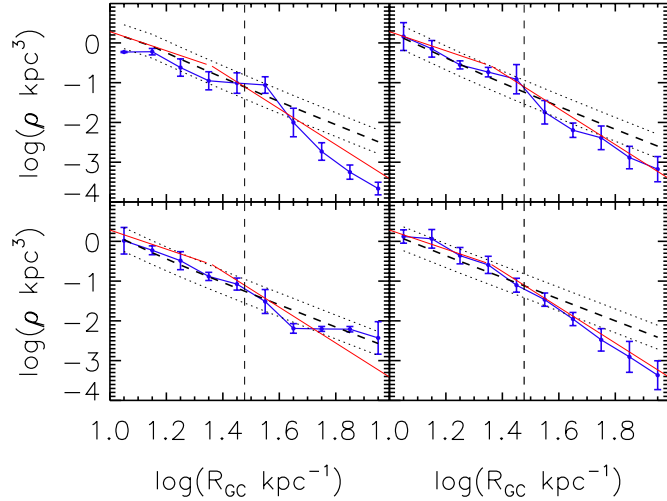


**Figure 14.** Radial number density profiles for four regions in R.A.:  $30^\circ < \text{R.A.} < 60^\circ$  (top left),  $0^\circ < \text{R.A.} < 30^\circ$  (top right),  $340^\circ < \text{R.A.} < 0^\circ$  (bottom left), and  $310^\circ < \text{R.A.} < 340^\circ$  (bottom right). The bottom left panel contains the Pisces overdensity at  $R_{\text{GC}} \sim 80$  kpc ( $\log(R_{\text{GC}}) \sim 1.9$ ). The symbols show the observed median number density and the rms scatter around the median value for pixels shown in Figure 11 (top). The dashed line shows the number density predicted from the smooth model ( $\log(\rho_{\text{model}}^{\text{RR}})$ , Equation (16)), and the dotted lines show the  $\pm 0.3$  dex envelope (a factor of 2) around the predicted values which corresponds to the sample Poisson noise determined from model-based number density maps. The solid line shows the prediction from Watkins et al. (2009). The  $\rho_{\odot}^{\text{RR}}$  in Equation (16) was increased by 33% to  $5.6 \text{ kpc}^{-3}$  to match the observations, and Watkins et al. (2009) predictions (their Equation (12)) had to be scaled down by a factor of 10 (assuming that their normalization was meant to be in units of stars per  $\text{kpc}^3$ ). The vertical line is added to guide the eye and shows the  $R_{\text{GC}} = 30$  kpc.

(A color version of this figure is available in the online journal.)

down their normalization, taken from their arXiv posting, by a factor of 10).

The apparent good agreement between the data and smooth, Jurić et al. (2008) halo model in the  $340^\circ < \text{R.A.} < 0^\circ$  direction at  $\sim 80$  kpc (Figure 14 bottom left panel) is due to Pisces overdensity.

To quantify the statistical significance of the underdense regions relative to a smooth model, we have divided stripe 82 into six regions, and for each computed the expected number of RR Lyrae stars by integrating  $\rho_{\text{model}}^{\text{RR}}$ . The statistical significance of the underdense regions is calculated by finding the absolute difference between the observed ( $N_{\text{obs}}$ ) and expected ( $N_{\text{exp}}$ ) number of RR Lyrae stars (based on the oblate halo model, Equation (16)), then dividing it by the Poisson uncertainty ( $\sqrt{N_{\text{exp}}}$ ). The results are presented in Table 5; the underdense

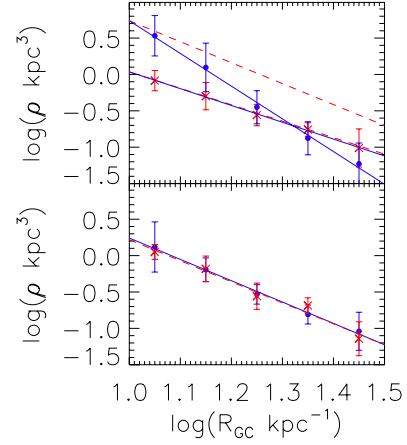


**Figure 15.** Top: radial number density profiles of Oo I (crosses) and Oo II RRab stars (dots) in the  $340^\circ < \text{R.A.} < 30^\circ$  direction. The symbols show the observed median number density and the rms scatter around the median value. The best-fit power laws to the data (power-law indices of  $-2.3$  and  $-4.5$ ) are shown as solid lines, with the Miceli et al. (2008) power laws overplotted as dashed lines. Bottom: radial number density profiles of RRab (dots) and RRc stars (crosses) in the  $340^\circ < \text{R.A.} < 30^\circ$  direction. The best-fit power laws (solid and dashed lines) have consistent power-law indices ( $-2.9$ ).

(A color version of this figure is available in the online journal.)

regions are statistically significant at the  $(1-3)\sigma$  level compared to the oblate halo model (Equation (16)). These underdensities cannot be explained by incompleteness as a function of apparent magnitude (since there are dozens of RR Lyrae detected up to 100 kpc in the Pisces stream region) or angle (because SDSS provides very homogeneous coverage of the sky). The simplest interpretation is that the spatial profile steepens at  $\sim 30$  kpc. This hypothesis is also supported by the distribution of halo main-sequence stars, discussed in Section 5.

Using the selection criteria from Section 4.6, we have divided the sample of RRab stars into Oosterhoff I (Oo I, 289 stars) and Oosterhoff II (Oo II, 77 stars) subsamples and compared their radial profiles in Figure 15 (top). In the direction that does not overlap with the Sgr tidal stream and the Hercules–Aquila Cloud ( $340^\circ < \text{R.A.} < 30^\circ$ ), and for  $R_{\text{GC}} < 30$  kpc, the Oo I subsample shows a shallower profile than the Oo II subsample. The best-fit power-law indices are  $-2.3$  and  $-4.5$ , respectively. The fit for the Oo I subsample is in excellent agreement with the result by Miceli et al. (2008) obtained over a much larger sky area ( $1430 \text{ deg}^2$  versus  $\sim 300 \text{ deg}^2$ ). For the Oo II subsample, our best fit is steeper (Miceli et al. obtained a best-fit index of  $-2.9$ ). The number of stars with

**Table 5**  
Poisson Statistics for RR Lyrae Detection in Six Stripe 82 Regions

Region	$N_{\text{exp}}^a \pm \sigma^b$	$N_{\text{obs}}^c$	Statistical Significance <sup>d</sup>	
$50 < d/\text{kpc} < 75$	$30^\circ < \text{R.A.} < 60^\circ$	$12 \pm 4$	2	2.5
	$0^\circ < \text{R.A.} < 30^\circ$	$10 \pm 3$	6	1
	$310^\circ < \text{R.A.} < 340^\circ$	$19 \pm 4$	8	3
$75 < d/\text{kpc} < 100$	$30^\circ < \text{R.A.} < 60^\circ$	$9 \pm 3$	0	3
	$0^\circ < \text{R.A.} < 30^\circ$	$8 \pm 3$	3	1.5
	$310^\circ < \text{R.A.} < 340^\circ$	$14 \pm 4$	4	2.5

**Notes.**

<sup>a</sup> Expected number of RR Lyrae calculated by integrating Equation (16).

<sup>b</sup> Uncertainty in the number of expected RR Lyrae calculated as  $\sqrt{N_{\text{exp}}}$ .

<sup>c</sup> Observed number of RR Lyrae.

<sup>d</sup> Statistical significance in units of  $\sigma$ , calculated as  $|N_{\text{exp}} - N_{\text{obs}}|/\sigma$ .

**Table 6**

Positions and Derived Parameters of RR Lyrae Stars in the Sagittarius and Pisces Streams

Stream	(R.A.) <sup>a</sup>	$\langle d \rangle^b$	$N_{ab}^c$	$N_c^c$	$N_{Oo\ I}^c$	$N_{Oo\ II}^c$	$\langle P \rangle_{ab}^d$	$\langle u - g \rangle_{\min}^e$
Sagittarius	30°	25	38	7	29	9	0.6	$1.13 \pm 0.01$
Pisces	355°	80	15	1	15	0	0.6	$1.12 \pm 0.06$

**Notes.**<sup>a</sup> Median equatorial J2000.0 right ascension.<sup>b</sup> Median heliocentric distance in kpc.<sup>c</sup> Number of type *ab*, *c*, Oo I, and Oo II RR Lyrae stars.<sup>d</sup> Median period of RRab stars in days.<sup>e</sup> Median  $\langle u - g \rangle_{\min}$  color of RR Lyrae stars and the uncertainty in the median.

$R_{GC} > 30$  kpc is too small (only 23 Oo II stars) to robustly measure the profile difference beyond the 30 kpc. We also note that the radial number density profiles of RRab and RRC stars have consistent best-fit power-law indices ( $-2.9$ ), as shown in Figure 15 (bottom). Interestingly, the Hercules–Aquila Cloud seems to be dominated by Oo I stars; the Pisces stream includes only Oo I stars.

**4.6. Period–Amplitude Distribution**

As suggested by Catelan (2009), the period–amplitude distribution of RR Lyrae stars may hold clues about the formation history of the Galactic halo. Catelan points to a sharp division (a dichotomy first noted by Oosterhoff 1939) between Oosterhoff type I (hereafter Oo I, average periods of RRab stars  $\langle P_{ab} \rangle \sim 0.55$  days), and Oosterhoff type II (hereafter Oo II, average periods of RRab stars  $\langle P_{ab} \rangle \sim 0.65$  days) globular clusters, with only very few clusters in between. On the other hand, the dSph satellite galaxies and their globular clusters fall preferentially on the “Oosterhoff gap” ( $0.58 < \langle P_{ab} \rangle < 0.62$ ; see his Figure 5). In light of these findings, it is interesting to examine the period–amplitude distribution of stripe 82 RR Lyrae stars in general, and the position of RR Lyrae stars from the Sgr and Pisces streams in particular, in the period–amplitude diagram.

The period–amplitude (or Bailey) diagram for RR Lyrae stars listed in Table 2 is shown in Figure 16. The stars are separated by the “quality” of their *g*-band light curves. A star with a low-quality light curve (a lot of scatter around the best-fit template,  $\zeta > 2.3$ ) may indicate a Blazhko variable RR Lyrae star. The data points are color-coded by the median *g* – *r* color at minimum brightness ( $\langle g - r \rangle_{\min}$ ) and by a template parameter  $\phi_{0.8}^g$  (which measures the rise time).

We find that  $\langle g - r \rangle_{\min}$  of RRab and RRC stars becomes redder (effective temperature at minimum brightness decreases) as the period of pulsation increases (cooler stars pulsate more slowly). The *g*-band light curve shape (i.e., the best-fit template) for RRab stars correlates strongly with the amplitude (and period), becoming on average more asymmetric ( $\phi_{0.8}^g$  increases) with increasing amplitude (and decreasing period). Using a linear fit, we find that the expression

$$\phi_{0.8}^g = 0.961 + 0.070A_g - 0.249P \quad (20)$$

reproduces the template measured  $\phi_{0.8}^g$  with an rms scatter of 0.025 (the measurement error for  $\phi_{0.8}^g$  is  $\sim 0.01$ ). The distribution of light curve shapes for RRab stars appears to be continuous.

The shape of RRC stars, on the other hand, appears to be bimodal, a finding supported by the light curves shown in Figure 17. We emphasize that this conclusion is independent

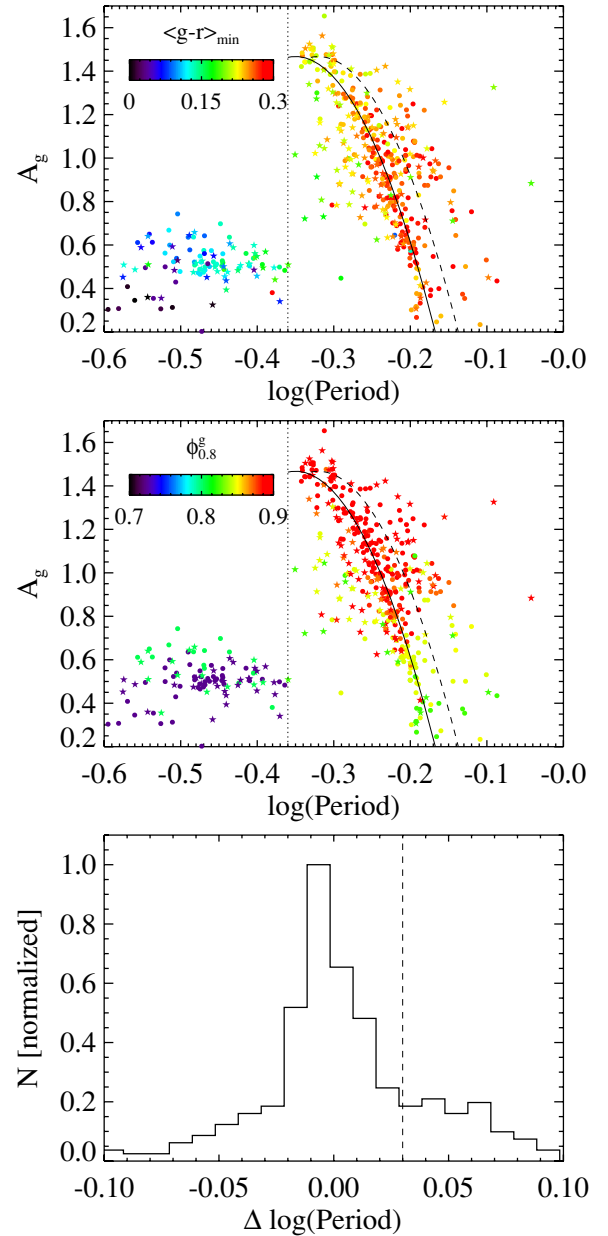


**Figure 16.** Period–amplitude diagram for RR Lyrae stars with high ( $\zeta < 2.3$ , circles) and low-quality *g*-band light curves ( $\zeta > 2.3$ , stars), color-coded by the median *g* – *r* color at minimum brightness ( $\langle g - r \rangle_{\min}$ ) in the top panel, and by  $\phi_{0.8}^g$  in the middle panel. The vertical line at  $\log(\text{Period}) = -0.36$  (10.5 hr) divides the RRC (first overtone, to the left) and RRab stars (fundamental mode, to the right). The solid line shows the position of the Oo I locus, while the dashed line (offset by 0.03 in the  $\log(\text{Period})$  direction from the Oo I locus line) separates the Oo I (to the left) and Oo II RRab stars (to the right). The position of the dashed line was determined from the  $\Delta \log(\text{Period})$  histogram (bottom), where  $\Delta \log(\text{Period})$  is the  $\log(\text{Period})$  distance (at constant amplitude) from the Oo I locus line. The *g*- and *r*-band light curves for the star with  $A_g \sim 1.3$  and  $\log(\text{Period}) \sim -0.09$  are shown in Figure 7.

of template fitting; the only information needed to fold the light curves in this figure is the best-fit period. The RRC stars with more asymmetric shapes ( $\phi_{0.8}^g \sim 0.8$ , dashed line template in Figure 6 bottom panel) also have on average higher *g*-band amplitudes than RRC stars with more symmetric curves (by  $\sim 0.1$  mag). These trends for RRab stars have been known for some time (in the Johnson *UBVRI* photometric system; Sandage et al. 1981), while the strong bimodality in the *g*-band light curve shape of RRC stars is apparently a new result.

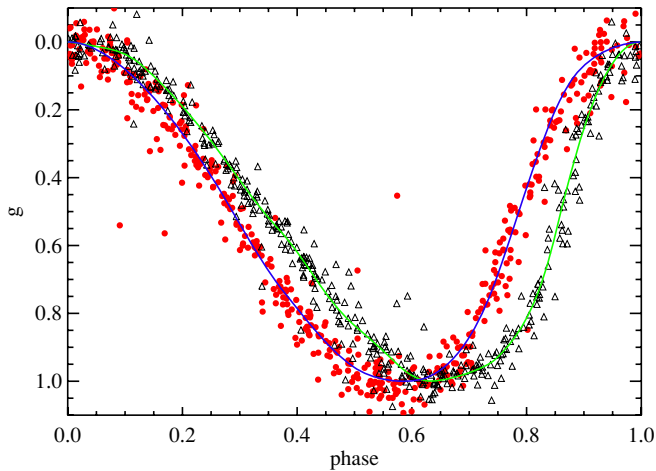


**Figure 17.** Symbols show high-quality  $g$ -band light curves (normalized and period-folded) of RRc stars fitted with template 0 (eight stars, dots) and 1 (nine stars, triangles), with templates shown as solid lines. The template 0 and 1 are also shown as the solid and dashed lines in Figure 6 (bottom). This bimodal distribution of observed light curves suggests that  $c$ -type RR Lyrae stars may include two distinct subtypes.

(A color version of this figure is available in the online journal.)

The period–amplitude distribution of RRab stars in Figure 16 appears to be bimodal, with the two groups possibly being Oosterhoff type I and type II stars. We fit a quadratic line

$$A_g = -3.18 - 26.53 \log(\text{Period}) - 37.88 \log(\text{Period})^2 \quad (21)$$

to high-quality light curve stars in the main locus, and note that the fitted line is very similar to the Cacciari et al. (2005) period–amplitude line of M3 globular cluster RR Lyrae stars. Since M3 is the prototype Oo I globular cluster, we label the main locus as the Oo I locus. The stars with low-quality light curves are not used in this fit, as they are probably Blazhko variables that might not be observed at their maximum amplitude, and therefore tend to scatter toward lower amplitudes in the Bailey diagram. We calculate the period shift,  $\Delta \log(\text{Period})$  (the  $\log(\text{Period})$  distance at a constant amplitude from the Oo I locus line) as

$$\Delta \log(\text{Period}) = \log(\text{Period}) - \log(\text{Period interpolated from the Oo I locus}). \quad (22)$$

The distribution of  $\Delta \log(\text{Period})$  values is centered on  $\Delta \log(\text{Period}) = 0$  by definition (the position of the Oo I locus), and has a long-period tail. Even though we do not see the clearly displaced secondary peak that is usually associated with an Oo II component (see Figure 21 in Miceli et al. 2008), hereafter we will refer to stars in the long-period tail as Oo II stars. Assuming that the distribution around  $\Delta \log(\text{Period}) = 0$  is symmetric for Oo I stars, we define RRab stars with  $\Delta \log(\text{Period}) < 0.03$  as Oo I, and those with  $\Delta \log(\text{Period}) > 0.03$  as Oo II.

The period–amplitude distributions of RR Lyrae stars in the Sgr stream ( $15^\circ < \text{R.A.} < 44^\circ$ ,  $18 < d/\text{kpc} < 35$ ) and the Pisces stream ( $\text{R.A.} > 345^\circ$ ,  $\text{R.A.} < 0^\circ$ ,  $75 < d/\text{kpc} < 100$ ) are shown in Figure 18. The median periods of RRab stars observed in these two streams are listed in Table 6. The Sgr stream has nine RRab Oo II stars while the Pisces stream has none; if the Pisces stream had the same fraction of Oo II stars as the Sgr stream, four would be expected. We have already discussed the differences in the spatial profiles between Oo I and Oo II stars in Section 4.5, and provide evidence that Oo II stars have metallicities about 0.3 dex lower than Oo I stars in the following section.

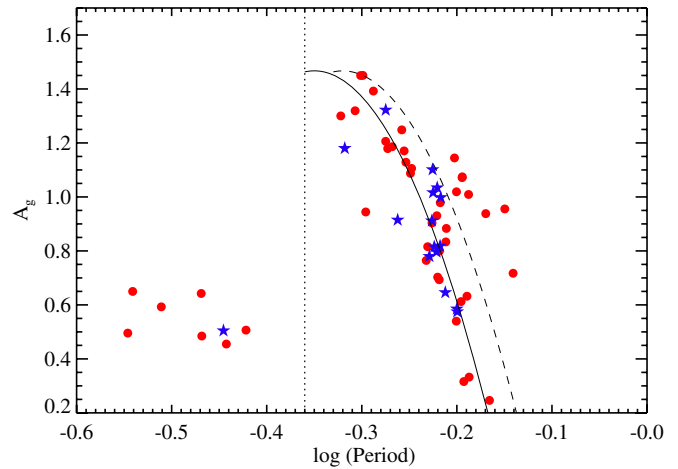


**Figure 18.** Period–amplitude diagram for RR Lyrae stars selected from the Sagittarius (dots) and Pisces streams (stars). The vertical line at  $\log(\text{Period}) = -0.36$  divides the RRc (first overtone, to the left) and RRab stars (fundamental mode, to the right). The solid line shows the position of the Oo I locus, while the dashed line (offset by 0.03 in the  $\log(\text{Period})$  direction from the Oo I locus line) separates the Oo I (to the left) and Oo II RRab stars (to the right).

(A color version of this figure is available in the online journal.)

#### 4.7. Metallicity Estimates for RR Lyrae Stars

In order to obtain a rough estimate of the metallicity of the Pisces and Sagittarius stream RR Lyrae stars, we consider several methods. The most accurate metallicity estimates for RR Lyrae stars ( $\pm 0.2$  dex; Vivas et al. 2008; Prior et al. 2009) can be obtained by employing the  $\Delta S$  method (Preston 1959), or one of its variants (Layden 1994), on the observed RR Lyrae spectra. In the absence of spectra, several photometric metallicity indices can be used, such as the ultraviolet blanketing index (Sturch 1966), the Strömgren  $m_1$  index (Epstein & Epstein 1973), or the Walraven system (Blanco 1992 and references therein). These photometric metallicity indices are less accurate than the spectroscopic estimates ( $\pm 0.5$  dex versus  $\pm 0.2$  dex), and are usually used when the stars of interest are faint, or when samples of RR Lyrae stars are large. Another method to estimate metallicity for RR Lyrae stars is based on the light curve shape, as discussed below.

##### 4.7.1. Photometric Metallicity

We now attempt to develop a photometric metallicity index similar to Sturch’s ultraviolet blanketing index, but based on the SDSS  $ugr$  bandpasses (instead of the Johnson  $UBV$  bandpasses). The basic idea behind this index is that the correlation between the  $U-B$  and  $B-V$  color at minimum brightness can be used to estimate the metallicity of an RRab star. The physics of this estimate is similar to that of photometric metallicity method used for main-sequence stars (Ivezić et al. 2008 and references therein).

In Figure 19 (top), we investigate if such a correlation exists between the  $u-g$  and  $g-r$  colors on a sample of 51 RRab stars with measured spectroscopic metallicities. The metallicities were obtained from SDSS spectra with the pulsation phase taken into account, and were processed through the SEGUE Spectral Parameters Pipeline (SSPP; Lee et al. 2008) by De Lee (2008), separately from the SDSS Data Release 7 spectra. The random uncertainty in the De Lee et al. spectroscopic metallicity is estimated at  $\sim 0.3$  dex, with systematic uncertainties of a similar magnitude. We have compared the De Lee et al. metallicity values to phase-averaged values listed as part of the SDSS Data

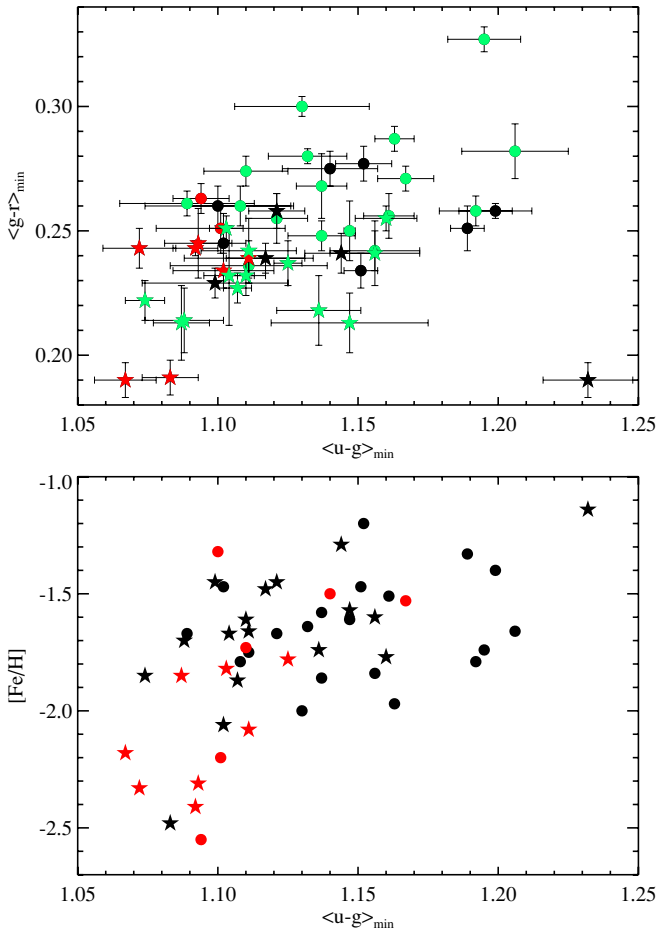


**Figure 19.** Top:  $\langle u - g \rangle_{\min}$  vs.  $\langle g - r \rangle_{\min}$  diagram for 51 RRAb stars with high- (dots) and low-quality  $g$ -band light curves (stars), and with spectroscopic metallicity measurements. The spectroscopic metallicities were obtained by De Lee (2008) from SDSS spectra processed with the SEGUE Spectroscopic Parameters Pipeline (SSPP; Lee et al. 2008). The  $\langle u - g \rangle_{\min}$  and  $\langle g - r \rangle_{\min}$  (symbols) show median colors at minimum brightness ( $0.5 < \text{phase} < 0.7$ ), and the error bars show errors in the median. The symbols are color-coded according to spectroscopically determined metallicity:  $[\text{Fe}/\text{H}] < -2.0$  (red),  $-1.5 < [\text{Fe}/\text{H}] < -2.0$  (green), and  $[\text{Fe}/\text{H}] > -1.5$  (black). Bottom: distribution of Oo I (black symbols) and Oo II (red symbols) RRAb stars with high- (dots) and low-quality  $g$ -band light curves (stars) in the  $[\text{Fe}/\text{H}]$  vs.  $\langle u - g \rangle_{\min}$  diagram. The Oo II stars are on average more metal-poor ( $[\text{Fe}/\text{H}] \sim -2.0$ ) and bluer in  $\langle u - g \rangle_{\min}$  ( $\langle u - g \rangle_{\min} \sim 1.1$ ) than the Oo I stars ( $[\text{Fe}/\text{H}] \sim -1.7$ ).

(A color version of this figure is available in the online journal.)

Release 7 and found a median offset of  $-0.15$  dex and rms scatter of 0.2 dex.

The conclusion derived from data shown in Figure 19 is that the most metal-poor RR Lyrae ( $[\text{Fe}/\text{H}] < -2.0$ ) usually have  $\langle u - g \rangle_{\min} < 1.11$ . These metal-poor stars are also predominantly classified as Oo II stars, as shown in Figure 19 (bottom). The median  $\langle u - g \rangle_{\min}$  of RRAb stars in the Pisces and Sagittarius streams is  $\sim 1.13$  mag, resulting in a weak constraint that their metallicities are in the range  $-2.0 < [\text{Fe}/\text{H}] < -1.5$  (on the De Lee metallicity scale).

Motivated by the  $[\text{Fe}/\text{H}]$  versus  $u - g$  color distribution shown in the bottom panel of Figure 19, we tried to estimate the photometric metallicity using only the  $\langle u - g \rangle_{\min}$  color. We first compute the median spectroscopic metallicity in 0.02 wide steps of the  $\langle u - g \rangle_{\min}$  color, from  $\langle u - g \rangle_{\min} = 1.07$  to  $\langle u - g \rangle_{\min} = 1.25$ , then fit a parabola to these medians (see

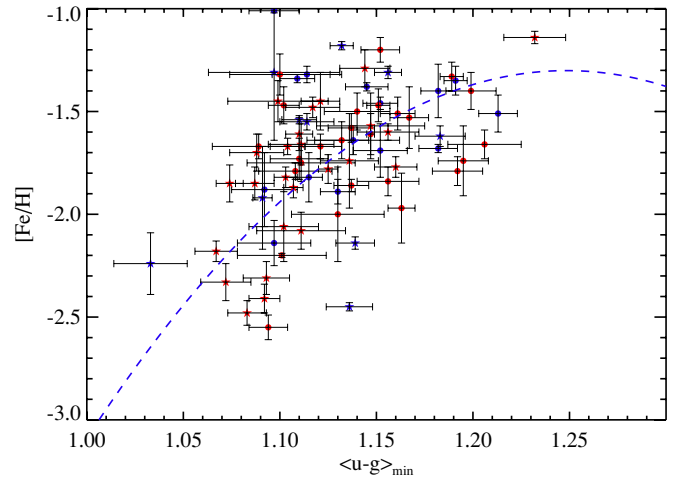


**Figure 20.** Dependence of spectroscopic metallicity on median  $u - g$  color at minimum brightness ( $\langle u - g \rangle_{\min}$ ) for RRAb (red symbols) and RRc (blue symbols) stars with high- (dots) and low-quality  $g$ -band light curves (stars). The best fit to median  $[\text{Fe}/\text{H}]$  values in 0.02 wide  $\langle u - g \rangle_{\min}$  bins is  $[\text{Fe}/\text{H}]_{\text{photo}} = -46.47 + 72.36\langle u - g \rangle_{\min} - 28.98\langle u - g \rangle_{\min}^2$  (dashed line). The spectroscopic metallicity errors are from De Lee (2008), but were not used in the fit as they are most probably underestimated (they should be  $\sim 0.3$  dex; De Lee 2008, private communication). The rms scatter of 76 individual data points around this line is 0.3 dex, and is consistent with the expected intrinsic scatter in spectroscopic metallicity.

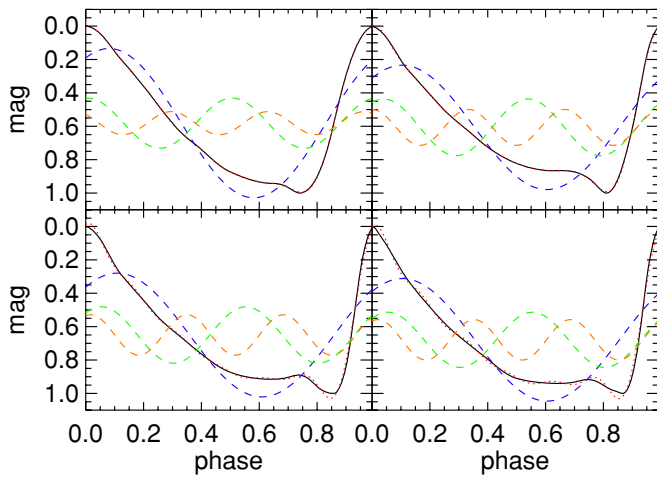
(A color version of this figure is available in the online journal.)

Figure 20). The best-fit expression is

$$[\text{Fe}/\text{H}]_{\text{photo}} = -46.47 + 72.36\langle u - g \rangle_{\min} - 28.98\langle u - g \rangle_{\min}^2. \quad (23)$$

In the validity range  $1.05 < \langle u - g \rangle_{\min} < 1.20$ , the best-fit values vary from  $-2.4$  to  $-1.4$ ; the largest value of the derivative of the best-fit is 0.1 dex/0.01 mag for  $\langle u - g \rangle_{\min} = 1.07$ . Of course, the absolute metallicity error (systematic error) in this expression is inherited from the input data provided by De Lee et al.; it could be as large as several times 0.1 dex. We emphasize that this estimator should not be applied outside the color range  $1.05 < \langle u - g \rangle_{\min} < 1.20$ , and that the large scatter of the calibration sample around the best-fit relation ( $\sim 0.3$  dex) should be noted.

Equation (23) predicts  $[\text{Fe}/\text{H}]_{\text{photo}} \sim -1.7$  dex for the metallicity of both the Sgr and Pisces streams. A similar value was obtained by Vivas et al. (2005) from spectroscopic observations of RR Lyrae stars in the *leading arm* of the Sagittarius tidal stream. However, the Equation (23) result for the *trailing arm* of the Sgr stream (discussed here) is lower by 0.5 dex than its metallicity obtained using halo main-sequence stars (in Section 5.1 below). A possible explanation for this discrepancy may be a systematic offset in the SSPP metallicity scale for hotter stars. For 45 RR Lyrae from the Sgr tidal stream ( $15^\circ < \text{R.A.} < 44^\circ$ ,  $18 \text{ kpc} < d < 35 \text{ kpc}$ ), we find using the SDSS DR7 SSPP data a median radial velocity of  $-150 \text{ km s}^{-1}$  (with an rms scatter of  $35 \text{ km s}^{-1}$ , indicating a fairly cold stream), and a median metallicity of  $[\text{Fe}/\text{H}] = -1.5$  (rms scatter of 0.2 dex). If the true median metallicity of the Sgr tidal stream (trailing arm) is  $[\text{Fe}/\text{H}] = -1.2$ , as suggested in Section 5.1, then the SSPP underestimates the metallicities of RR Lyrae (and possibly blue horizontal-branch) stars by 0.3 dex. The combination of this  $-0.3$  dex offset and a  $-0.15$  dex offset between the DR7 and De Lee metallicities could explain the 0.5 dex difference between the median metallicity based on Equation (23) and the main sequence-based value obtained



**Figure 21.** Examples of best-fit Fourier expansion with six *sine* terms to light curve templates for *ab*-type RR Lyrae stars. The solid line shows the template, and the three dashed lines show the first three harmonics (offset for clarity). The sum of all six harmonics is shown by the dotted line (barely visible and close to the solid line). These four examples span the full range of the minimum phase, ranging from 0.75 in the top left panel to 0.87 in the bottom right panel. For fixed values of period and amplitude, the phase of the minimum increases as the metallicity decreases.

(A color version of this figure is available in the online journal.)

in the following section. The SSPP results for hotter stars are presently being refined, based on comparisons with high-resolution spectroscopy, and this may resolve the apparent discrepancy in the near future.

#### 4.7.2. Relationship between Metallicity and Light Curve Shape

Another potentially useful method for estimating the metallicity of RR Lyrae stars is based on the Fourier decomposition of light curves (Jurcsik & Kovács 1996). Their result that the Fourier parameters are correlated with the metallicity (see also Kunder & Chaboyer 2008) for an independent confirmation of this correlation) implies that our templates should also correlate with metallicity. Furthermore, they have established that the expansion coefficients are well correlated among themselves, which is consistent with our finding that light curves are essentially a one-dimensional family.

Following Simon & Clement (1993), Jurcsik & Kovács (1996) parameterized their metallicity–light curve shape relation using the phase of the third harmonic (for the *sine* expansion),  $\phi_{31}$ . We have expanded our type-*ab* templates using six *sine* terms (the fitting residuals for five terms are still comparable to our template errors, and more than six terms does not result in substantial best-fit improvement) and found a nearly perfect relation between our *g*-band template light curve parameterization ( $\phi_{0.8}^g$ ) and the Fourier expansion ( $\phi_{31}$ ):

$$\phi_{31} = -6.64\phi_{0.8}^g + 10.81, \quad (24)$$

which reproduces directly measured  $\phi_{31}$  (from the Fourier expansion) with an rms of 0.07 (a typical fractional error of 1%–2%), roughly the same as the error in  $\phi_{31}$  due to the template error for  $\phi_{0.8}^g$  ( $\sim 0.01$ ). Examples of the best Fourier fits to our templates are shown in Figure 21. It is evident that the third harmonic controls the position of the light curve minimum, which in turn determines the value of  $\phi_{0.8}^g$ .

With this relation, we can now compute the metallicity estimates using the Sandage (2004) expression (given on the Zinn & West (1984) scale; the Jurcsik & Kovács scale is about

0.3 dex more metal-rich):

$$[\text{Fe}/\text{H}]_{\text{San04}} = -5.49 - 5.664P + 1.412\phi_{31}. \quad (25)$$

This expression is valid for  $P > 0.43$  days and  $4.7 < \phi_{31} < 5.7$ , and has a precision of 0.2 dex. The difference between the  $[\text{Fe}/\text{H}]_{\text{San04}}$  and the SDSS spectroscopic metallicity for 51 stars with the latter data has a median offset of  $-0.07$  dex and rms scatter of 0.33 dex. Given that the errors in SDSS values are about 0.3 dex, the agreement is satisfactory. Indeed, it is encouraging that the median offset is so small given that the methods and their calibration are entirely independent.

Using the SDSS metallicity for 51 stars, we have also determined a best-fit linear combination of period, *g*-band amplitude and  $\phi_{31}$

$$[\text{Fe}/\text{H}]_{\text{SDSS}} = -0.66 - 3.65P - 0.493A_g + 0.313\phi_{31} \quad (26)$$

which reproduces the spectroscopic metallicity with an rms scatter of 0.26 dex. The scatter is smaller than for  $[\text{Fe}/\text{H}]_{\text{San04}}$  because Equation (26) is directly fit to the data. On average,  $[\text{Fe}/\text{H}]_{\text{SDSS}}$  is 0.1 dex higher than  $[\text{Fe}/\text{H}]_{\text{San04}}$ , with an rms scatter of their difference of only 0.13 dex; hence, the two expressions are practically equivalent. Equation (26), together with Equation (24), implies that for fixed values of period and amplitude, the phase of the light curve minimum increases as the metallicity decreases; on average, low-metallicity RR Lyrae have shorter rise time than metal-rich RR Lyrae.

With the light curve based metallicity given by Equation (26), we revisited the  $[\text{Fe}/\text{H}]$  versus  $u - g$  relationship given by Equation (23) using a six times larger and much less selection-biased sample. The results show a much smaller gradient of the  $u - g$  color with metallicity, about  $0.02 \text{ mag dex}^{-1}$ , and call in question the reliability of the photometric metallicity estimator given by Equation (23).

Using metallicity estimates computed by Equations (23) and (25), we have compared the metallicity distribution of RR Lyrae in the Sgr and Pisces streams to the rest of the sample. To within 0.05 dex, there is no detectable difference. On the other hand, the light curve based metallicity distributions for Oo I and Oo II stars are different. The median metallicity for Oo I stars is 0.31 dex higher when using Equation (23), and 0.46 dex higher when using Equation (25). However, both the separation of Oo I from Oo II stars, and the light curve based metallicity use the information about period and amplitude (e.g., a large period results in Oo II classification and low metallicity). A somewhat smaller, but still significant ( $\sim 2\sigma$ ) difference in the median metallicity of 0.2 dex is found between 37 Oo I stars and 14 Oo II stars with available spectroscopic metallicities.

We have also tested light curve-based metallicity estimates using a sample of 11 RR Lyrae stars with accurate light curves, and for which there are reliable spectroscopic metallicities (Vivas et al. 2008). We fit our *g*-band template set to their light curves, and apply Equations (25) and (26) to compute  $[\text{Fe}/\text{H}]$ . The differences between these light curve-based metallicity estimates and spectroscopic values show an rms scatter of only 0.14 dex. The median offset is 0.23 dex, with the spectroscopic values being higher. This offset may indicate a need to recalibrate the Sandage relation for use with our templates, because both his relation and the spectroscopic metallicities are supposed to be tied to the Zinn & West (1984) scale.

In summary, given the strong correlations between independent light curve quantities, period, amplitude, and the shape parameter  $\phi_{31}$ , and the results of Jurcsik & Kovács (1996) and

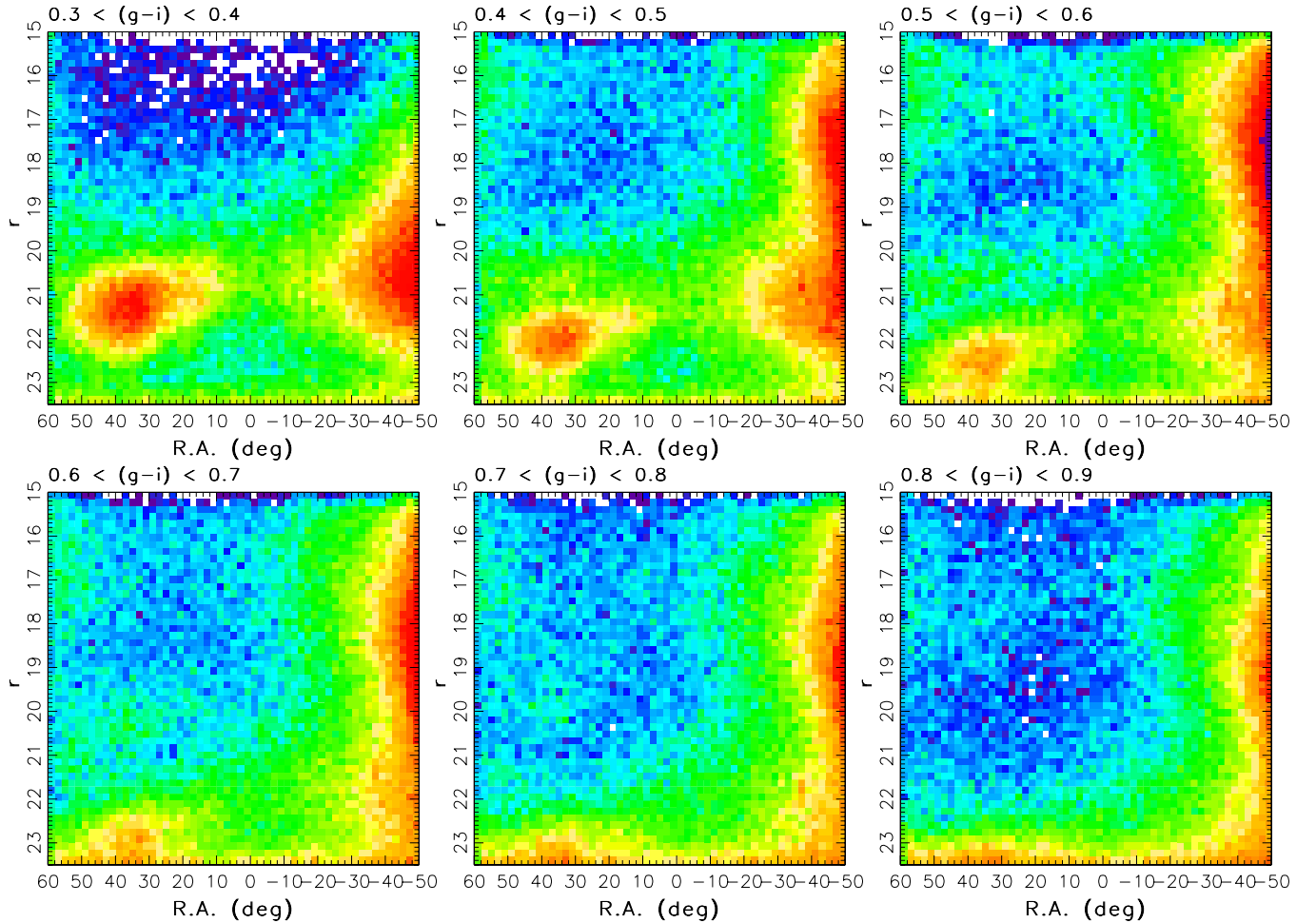


**Figure 22.** Stellar counts in deep co-added data from stripe 82. Each panel shows stars from a 0.1 mag wide  $g-i$  color bin, as marked on top, with the  $g-i$  color increasing from top left (0.3–0.4) to bottom right (0.8–0.9). Assuming  $[\text{Fe}/\text{H}] = -1.5$ , the median  $r$ -band absolute magnitude varies from  $M_r = 4.4$  to  $M_r = 6.6$ . The counts are shown on a logarithmic scale, increasing from blue to yellow and red (varying normalization for each panel to emphasize features). The red vertical features visible at the right edge of each panel are due to disk stars at  $r < 20$  and halo stars at fainter magnitudes (including the Hercules–Aquila Cloud). The stars in the well-defined overdensity at R.A.  $\sim 20^\circ$ – $50^\circ$  belong to the Sgr dSph tidal stream (trailing arm). The variation of apparent magnitude at which the overdensity is detected with the  $g-i$  color shows that these stars are on the main sequence (see Figure 23). The distance to the overdensity is in the 25–30 kpc range.

Kunder & Chaboyer (2008), it is likely that RR Lyrae light curves contain information about metallicity. However, the currently available spectroscopic subsample for the SDSS stripe 82 region is insufficient to convincingly demonstrate this relationship.

We note that Watkins et al. (2009), using essentially the same data set as we did, have claimed that the metallicity for RRab stars can be determined from SDSS light curves with an rms of 0.25 dex by applying the Jurcsik & Kovács method, in apparent conflict with our conclusions. A possible explanation for this discrepancy is that they fit a large number of free parameters (eight) to small samples of stars ( $\sim 100$ ). We have used the same functional form as proposed by Watkins et al. (2009) to fit *randomly* generated values for  $[\text{Fe}/\text{H}]$  and other parameters. In 20%–30% of simulated cases, we obtain very similar distributions in the  $[\text{Fe}/\text{H}]_{\text{fit}}$  versus  $[\text{Fe}/\text{H}]_{\text{input}}$  diagrams as those shown by Watkins et al. (2009).

## 5. THE DISTRIBUTION OF MAIN-SEQUENCE STARS IN STRIPE 82

The strength of the evidence for a steepening of the halo stellar number density profile discussed in Section 4.5 is limited by the small size of the RR Lyrae sample, as well as by difficulties

associated with using RR Lyrae stars as tracers (see Section 1). A more robust case can be made by tracing the distribution of the much more numerous main-sequence stars, using an approach such as that discussed by Jurić et al. (2008). Over most of the SDSS area, the distribution of blue main-sequence stars can be mapped out to a distance limit of  $\sim 20$  kpc, which is insufficient to test the transition at  $\sim 30$  kpc. However, the co-added stripe 82 data (J. Annis et al. 2009, in preparation) have a limiting magnitude about 2 mag fainter than single-epoch SDSS data, and can be used to map the number density distribution of blue main-sequence stars out to  $\sim 40$  kpc.

Figure 22 shows the distribution of stars, in several narrow color ranges, as a function of apparent magnitude and position along the stripe 82. In each color bin, stars have approximately the same absolute magnitude, thus more distant stars are fainter. The data clearly show a well-defined isolated overdensity of stars at R.A.  $\sim 20^\circ$ – $55^\circ$ . As the color becomes redder the overdensity is detected at fainter magnitudes, ranging from  $r \sim 21$ – $22$  for the bluest bin and disappearing at the faint end ( $r \sim 23.5$ ) in the reddest bin. This behavior is consistent with the behavior of the main-sequence stars, as illustrated in the top middle panel in Figure 23.

The top right and bottom panels in Figure 23 exhibit qualitative evidence for the steepening of the halo density profile; in the

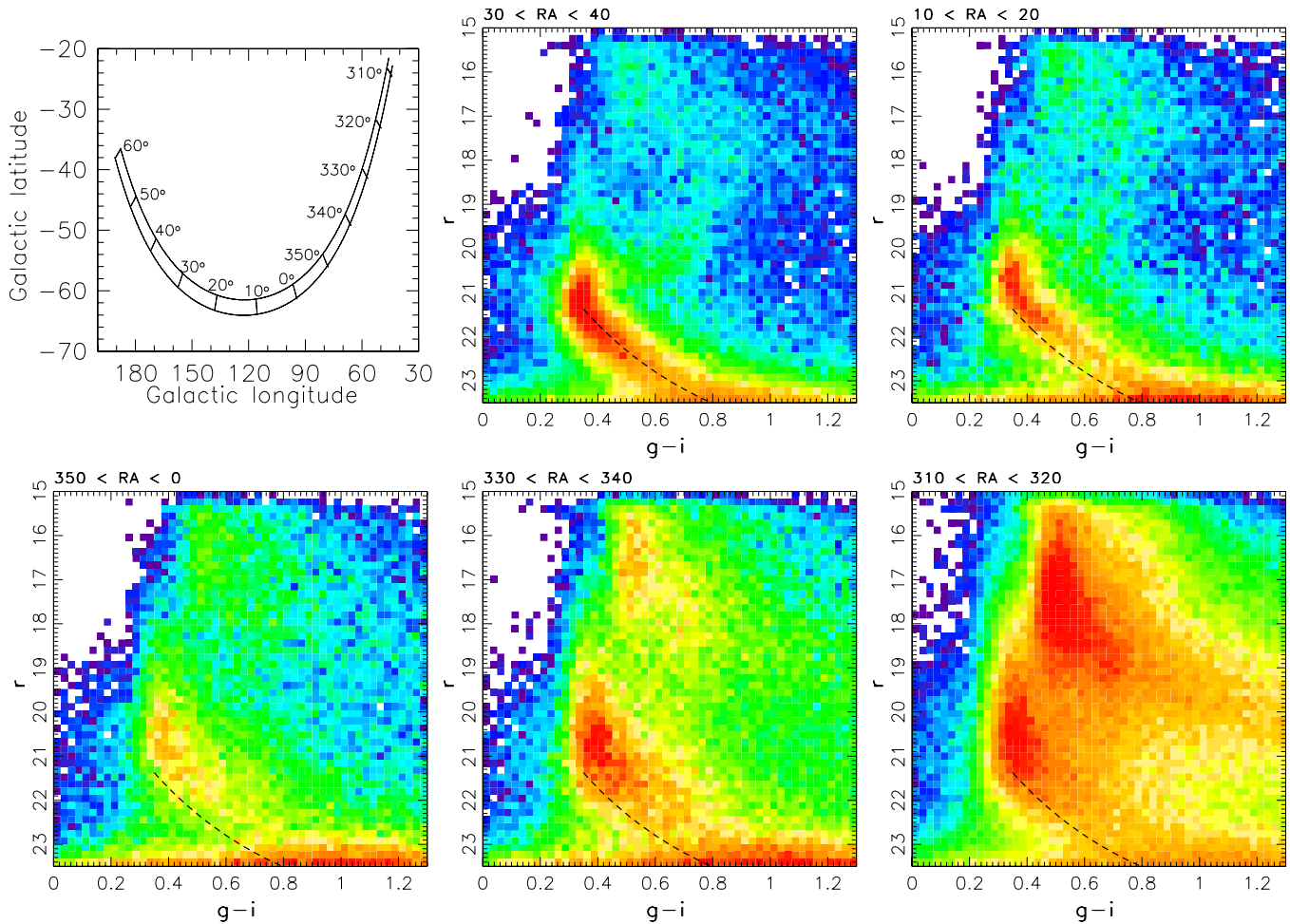


**Figure 23.** Top left panel shows the stripe 82 footprint in the galactic coordinates. The corresponding R.A. along the stripe is marked (decl.  $\sim 0$ ). The other five panels show the  $r$  vs.  $g-i$  color-magnitude (Hess) diagrams for five  $25 \text{ deg}^2$  large regions from stripe 82 selected by R.A. (the range is listed on the top of each panel). The top middle panel corresponds to a region intersecting the Sgr dSph tidal stream; note the MSTO at  $g-i \sim 0.3$  (F-type dwarfs) and a well-defined subgiant branch. The MSTO at  $g-i \sim 0.3$  indicates that the main-sequence stars in the Sgr trailing arm are at least 8 Gyr old. The counts are shown on a logarithmic scale, increasing from blue to yellow and red (with varying normalization to emphasize features). The dashed lines are added to guide the eye and to show the position of main-sequence stars with  $[\text{Fe}/\text{H}] = -1.2$  at a distance of 30 kpc. Note the lack of stars with  $g-i \sim 0.4$  and  $r > 22$  in most panels. For the median halo metallicity of  $[\text{Fe}/\text{H}] = -1.5$ ,  $r = 22$  corresponds to 28.7 kpc. The feature at  $g-i \sim 0.5$  and  $r \sim 15-18$  is due to thick disk stars.

color range  $0.3 < g-i < 0.5$ , and away from the Sgr stream, the differential counts of stars significantly decreases (by about a factor of 2) at magnitudes  $r > 22$ . If the density profile followed the canonical  $R^{-3}$  power law, the differential counts would be approximately constant. In order to quantitatively address this effect, we compare the observed counts to a simulated sample based on a smooth oblate halo model from Jurić et al. (2008). As shown in Figure 24, the model and data are in excellent agreement at galactocentric distances less than  $\sim 25$  kpc. However, at larger distances from the Galactic center, and outside the Sgr dSph tidal stream, the model *overpredicts* the observed counts by about a factor of 2. This mismatch strongly suggests that the halo stellar number density profile is much steeper beyond 30 kpc than given by the best-fit model from Jurić et al. (2008; which was constrained using stars at distances below 20 kpc). Unfortunately, due to the small stripe 82 area, and the effect of the Sgr dSph tidal stream on measured stellar counts, it is not possible to robustly derive precise quantitative adjustments to model parameters (e.g., there is a strong degeneracy between oblateness and density profile power-law index over such a small area). Nevertheless, this analysis provides *the first direct evidence* that the halo stellar number density is about a factor of 2 smaller than predicted by the Jurić et al. (2008)

model at  $\sim 30$  kpc from the Galactic center. As a rough estimate, in order to induce a factor of 2 difference in the count ratio as the galactocentric radius increases from 25 pc to 35 kpc, the power-law index has to decrease by about two (e.g., from  $R^{-3}$  to  $R^{-5}$ ). This estimate is consistent with the profiles shown in Figure 14 (beyond 30 kpc).

The bottom right panel in Figure 24 shows another overdensity at  $310^\circ < \text{R.A.} < 330^\circ$  and distances in the range 10–25 kpc (about a factor of 1.6 compared to the smooth halo model; the Sgr dSph tidal stream produces a peak overdensity of about a factor of 5). This overdensity appears to be the same structure as the Hercules–Aquila Cloud discovered by Belokurov et al. (2007b), and also seen in the distribution of RR Lyrae stars (Section 4.3).

### 5.1. The Metallicity of the Sgr dSph Tidal Stream (Trailing Arm)

Ivezić et al. (2008) developed a photometric metallicity estimator based on the  $u-g$  and  $g-r$  colors of main-sequence stars. The deep co-added stripe 82 data can be used to apply this method to a larger distance limit ( $\sim 20-30$  kpc) than for nominal SDSS data ( $\sim 10$  kpc), due to the decreased photometric errors. Figure 25 shows the median metallicity as a function of apparent

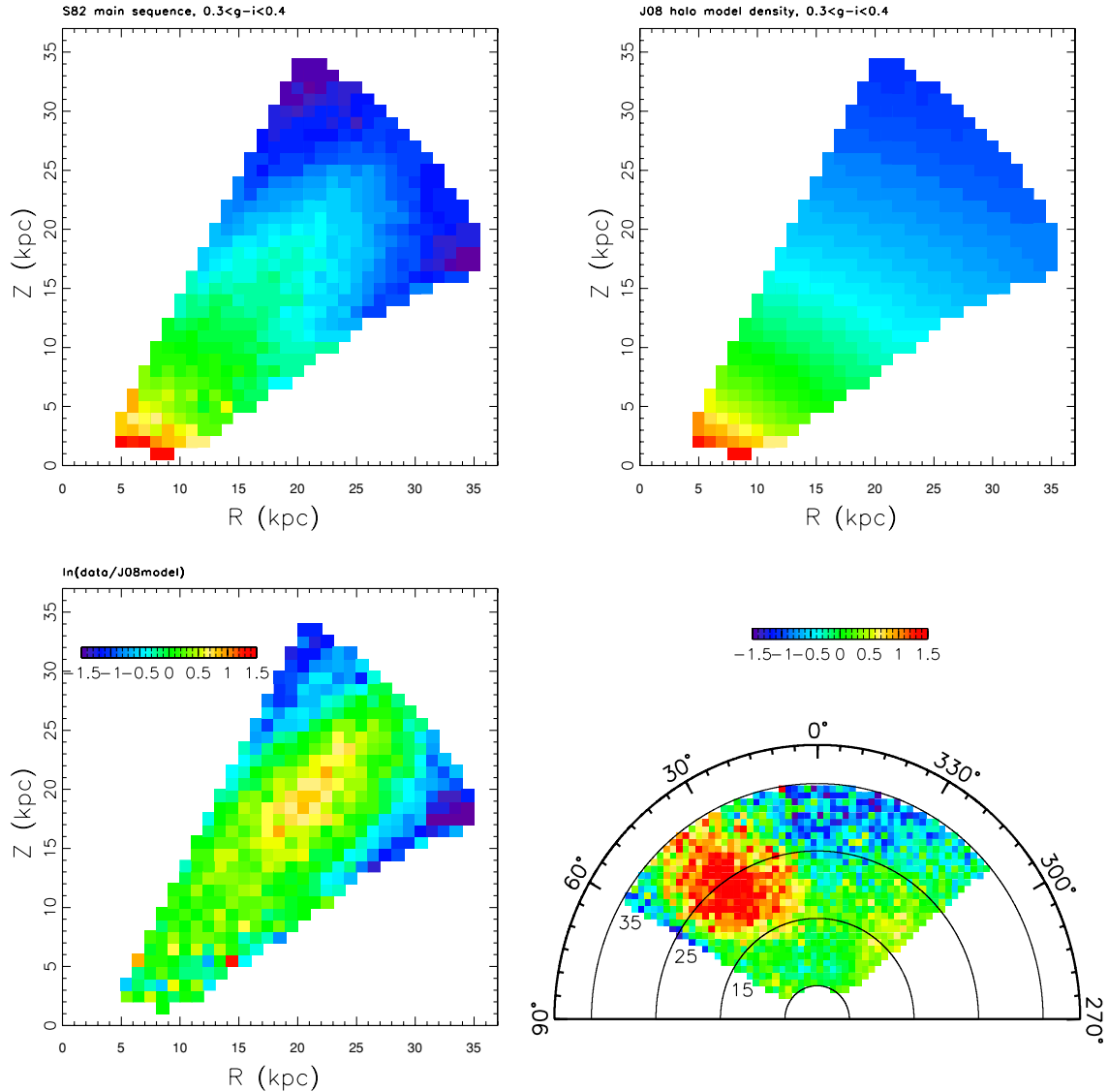


**Figure 24.** Comparison of the observed distribution of main-sequence stars in stripe 82 and predictions based on a smooth oblate halo model from Jurić et al. (2008). The top left panel shows the number density of stars with  $0.3 < g - i < 0.4$  on a logarithmic scale (increasing from blue to yellow and red) in a galactocentric cylindrical coordinate system (the Sun is at  $R = 8$  kpc,  $Z = 0$ ; all data are at negative  $Z$ ). The top right panel shows the model prediction. The bottom left panel shows the  $\ln(\text{data}/\text{model})$  map, color-coded according to the legend shown in the panel. The overdensity centered on ( $R \sim 20$  kpc,  $Z \sim 20$  kpc) is the Sgr dSph tidal stream (trailing arm). Note that at large distances from the Galactic center, and outside the Sgr dSph tidal stream, the model overpredicts the observed counts by about a factor of 2–3. At galactocentric distances  $\lesssim 20$  kpc, the model and data are in excellent agreement. The bottom right panel is analogous to the bottom left panel, except that the map is shown in stripe 82 coordinates, with the equatorial position angle (R.A.) marked on the top. The Sgr dSph tidal stream is seen at  $25^\circ < \text{R.A.} < 55^\circ$ , with the maximum value of the overdensity at about five. The Hercules–Aquila cloud is seen at  $310^\circ < \text{R.A.} < 330^\circ$ , and distances in the range 10–25 kpc, and represents a factor of  $\sim 1.6$  overdensity. The region with  $340^\circ < \text{R.A.} < 5^\circ$  and distances in the range 25–35 kpc represents a factor of  $\sim 2$  underdensity, relative to the Jurić et al. (2008) smooth halo model.

magnitude and position along the stripe 82. Throughout most of the volume, the median metallicity is  $[\text{Fe}/\text{H}] \sim -1.5$ , in agreement with results from Ivezić et al. (2008). However, in the region where the highest concentration of Sgr dSph tidal stream stars is found, the median metallicity is higher by 0.3 dex. On the other hand, the median metallicity in the Hercules–Aquila Cloud region is consistent with the median halo metallicity.

In regions outside the Sgr tidal stream, and for  $r > 21$ , there is evidence for a metallicity gradient, and for median values  $[\text{Fe}/\text{H}] < -1.5$ . We have analyzed the metallicity distribution for stars with  $320^\circ < \text{R.A.} < 350^\circ$  ( $l \sim 60^\circ$ ,  $b \sim -40^\circ$ ,  $0.3 < g - i < 0.4$ ), as a function of galactocentric radius. In the range 10–20 kpc, we find that the median metallicity decreases nearly linearly from  $[\text{Fe}/\text{H}] = -1.4$  (with an rms scatter of 0.33 dex) at 10 kpc, to  $[\text{Fe}/\text{H}] = -1.6$  (with an rms scatter of

0.8 dex, dominated by measurement errors) at 20 kpc. This is a larger gradient (0.02 dex/kpc) than the upper limit of 0.01 dex/kpc measured by Ivezić et al. (2008) at smaller galactocentric distances. This change of metallicity corresponds to a change of median  $u - g$  color (which provides the signal) from 0.92 mag at 10 kpc (rms scatter around the median is 0.06 mag) to 0.88 mag at 20 kpc (rms scatter around the median is 0.17 mag). Clearly, this measurement would greatly benefit from deeper  $u$ -band data.

The photometric metallicity measurement for the Sgr dSph tidal stream can be used to test a novel method for estimating the metallicity of spatially coherent substructures when the  $u$ -band data are *not* available. The absolute magnitudes of RR Lyrae and main-sequence stars have opposite dependence on metallicity, with RR Lyrae getting brighter and main-sequence stars getting

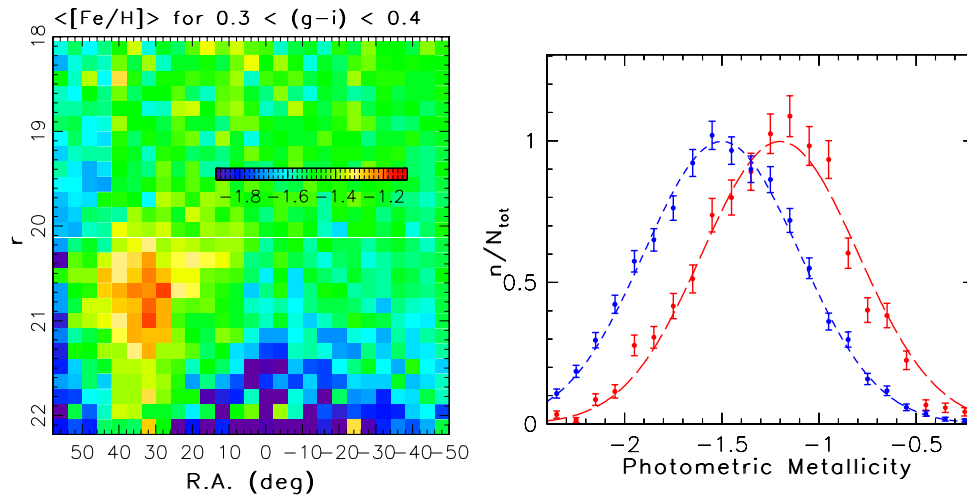


**Figure 25.** Left panel shows the median photometric metallicity for 88,000 stars with  $0.3 < g - i < 0.4$  and  $18 < r < 22.2$  in deep co-added data from stripe 82, as a function of apparent magnitude and position along the stripe. Note the relatively high metallicity ( $[Fe/H] \sim -1.20$ ) of the Sgr dSph tidal stream region (R.A.  $\sim 30^\circ$ – $40^\circ$  and  $20 < r < 21$ ). On the other hand, the median metallicity in the region with R.A.  $< -10^\circ$  and  $r > 20$ , where the Hercules–Aquila overdensity is found, is consistent with the median halo metallicity ( $[Fe/H] = -1.50$ ). The right panel compares the metallicity distributions for stars with  $20.5 < r < 21$  selected from two regions: 2200 stars with  $30^\circ < \text{R.A.} < 40^\circ$  (Sgr dSph tidal stream, right histogram) and 4500 stars with  $-40^\circ < \text{R.A.} < -10^\circ$  (control halo sample, left histogram). The dashed lines are best-fit Gaussians; both have widths  $\sigma = 0.4$  dex and are centered on  $[Fe/H] = -1.50$  (halo, left) and  $[Fe/H] = -1.20$  (Sgr dSph tidal stream, right).

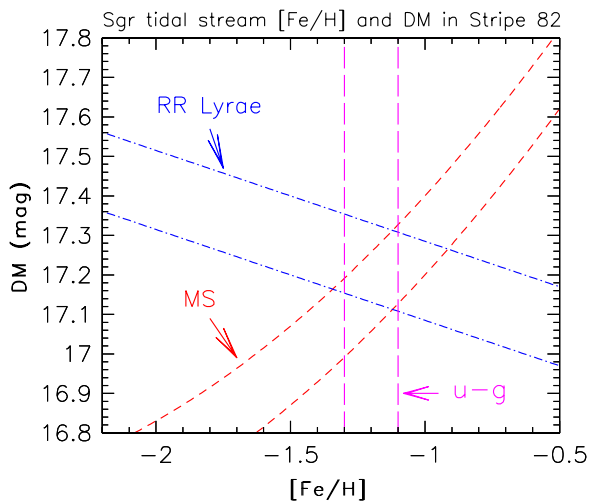


**Figure 26.** Summary of the constraints on the distance and metallicity of Sgr dSph tidal stream (trailing arm). The dot-dashed lines show a constraint obtained from the mode of the apparent magnitude distribution of RR Lyrae stars, with  $\pm 0.1$  mag adopted as the uncertainty. Diagonal short-dashed lines are analogous constraints obtained from the median apparent magnitude of main-sequence stars with  $0.4 < g - i < 0.5$ . The vertical long-dashed lines mark the median photometric metallicity for main-sequence stars, with  $\pm 0.1$  dex adopted as the uncertainty. All three constraints agree if the distance modulus is  $DM = 17.2$  mag and  $[Fe/H] = -1.2$ . A hypothesis that the Sgr dSph tidal stream (trailing arm) has the same metallicity as halo field stars ( $[Fe/H] = -1.5$ ) is strongly ruled out.

fainter with decreasing metallicity (see Equation (11) in this work and Equation A2 in Ivezić et al. 2008, respectively). With an assumption that both RR Lyrae stars and main-sequence stars are at the same distance and have the same metallicity in a well-defined overdensity such as the Sgr dSph tidal stream, then both distance and metallicity can be simultaneously determined. The application of this method to the Sgr dSph tidal stream (trailing arm) data is illustrated in Figure 26.

A slight difficulty in the application of this method comes from the small RR Lyrae sample size and the finite width of their apparent magnitude distribution. We have adopted the mode

(with 10 stars in a 0.5 mag wide bin) as a relevant statistic. The main-sequence stars are so numerous that the median and mode are indistinguishable. A consistent solution is obtained for a distance modulus of 17.2 mag (distance of 27.5 kpc) and  $[Fe/H] = -1.2$ .

It is encouraging that this metallicity is the same as obtained using the photometric metallicity method. The photometric metallicity estimate implies that, with the various error distributions taken into account, the metallicity difference between RR Lyrae and main-sequence stars in the Sgr trailing arm is not larger than 0.2 dex. We note that the photometric metallicity scale is tied to the SDSS spectroscopic metallicity scale for main-sequence stars.

In addition to similarity of their metallicity distributions, RR Lyrae and main-sequence stars in the Sgr trailing arm seem to have similar age distributions. The top middle panel in Figure 23 robustly shows the MSTO of the trailing arm at  $g - i \sim 0.3$  (F dwarfs). Together with the color–metallicity–age map shown in Figure 28 from An et al. (2009), this MSTO color and our metallicity estimate ( $[Fe/H] = -1.2$ ) indicate that the main-sequence population in the Sgr trailing arm is at least 8 Gyr old, and thus consistent with the presumed age of RR Lyrae stars.

In summary, if both RR Lyrae and main-sequence stars are detected in the same spatially coherent structure, the metallicity can be reliably estimated (to within  $\sim 0.1$  dex) by requiring the same distance modulus. We note that the calibration of both relevant absolute magnitude versus metallicity relations is based on available globular cluster data.

## 6. CONCLUSIONS AND DISCUSSION

We have presented the most complete sample of RR Lyrae stars identified so far in the SDSS stripe 82 data set, consisting of 379 RRab and 104 RRC stars. Our visual inspection of single-band and color light curves insures that the sample contamination is essentially negligible. Although the sky area is relatively small compared to other recent surveys, such as Keller et al. (2008) and Miceli et al. (2008), this RR Lyrae sample has the largest distance limit to date ( $\sim 100$  kpc).

In addition, a large number of well-sampled light curves in the *ugriz* photometric system have enabled the construction of a new set of empirical templates. This multi-band empirical template set provides strong constraints for models of stellar pulsations, through the single-band light curve shape, the shape variation with wavelength, and through the distributions of the templates. For example, while *ab*-type RR Lyrae appear to have a continuous distribution of light curve shapes, *c*-type RR Lyrae exhibit a clear bimodal distribution. This bimodality suggests that the latter class may include two distinct subclasses, which would be an unexpected result given that RR Lyrae stars have been carefully studied for over a century (e.g., Bailey 1903). A subclass of RR Lyrae stars with amplitudes and periods similar to the *c*-type, but with asymmetric light curves, has been noted in the MACHO data by Alcock et al. (1996). They suggested that these stars are pulsating in the second-harmonic mode.

Our accurate templates will greatly assist the identification of RR Lyrae stars in data sets with relatively small numbers of epochs. For example, all three major upcoming wide-area ground-based surveys plan to obtain fewer than 10 epochs (SkyMapper, Dark Energy Survey, and Pan-STARRS1  $3\pi$  survey), in the same photometric system. Without template fitting, the selection based on only low-order light-curve statistics includes a significant fraction ( $\sim 30\%$ ) of contaminants (dominated by  $\delta$  Scuti stars).

The high level of completeness and low contamination of our resulting sample, as well as the more precise distance estimates, enabled a more robust study of halo substructure than was possible in our first study. Our main result remains: the spatial distribution of halo RR Lyrae at galactocentric distances 5–100 kpc is highly inhomogeneous. The distribution of  $\rho/\rho_{\text{model}}^{\text{RR}}$  suggests that at least 20% of the halo within 30 kpc is found in apparently real substructures. Bell et al. (2008) find a lower limit of 40%, but they used a different metric and different tracers (turnoff stars). Schlaufman et al. (2009) have demonstrated that at least 34% of inner-halo (in their paper they explored regions up to 17 kpc from the Galactic center) MSTO stars are contained in structures they refer to as ECHOS (elements of cold halo substructures), based on an examination of radial velocities in the SEGUE sample. Thus, three separate studies, using very different probes, have come to essentially identical conclusions.

A comparison of the observed spatial distribution of RR Lyrae stars and main-sequence stars to the Jurić et al. (2008) model, which was constrained by main-sequence stars at distances up to 20 kpc, strongly suggests that the halo stellar number density profile steepens beyond  $\sim 30$  kpc. While various indirect evidence for this behavior, based on kinematics of field stars, globular clusters, and other tracers has been published (Carollo et al. 2007 and references therein), our samples provide a direct measurement of the stellar halo spatial profile beyond the galactocentric distance limit of  $\sim 30$  kpc. A similar steepening of the spatial profile was detected using candidate RR Lyrae stars by Keller et al. (2008). In addition to presenting new evidence for the steepening of halo stellar number density profile beyond  $\sim 30$  kpc, we have confirmed the result of Miceli et al. (2008) that the density profile for Oosterhoff II stars is steeper than for Oosterhoff I stars within 30 kpc.

We have analyzed several methods for estimating the metallicities of RR Lyrae stars. Using spectroscopic data processed with the SDSS SSPP pipeline as a training sample, we have established a weak correlation with the  $u - g$  color at minimum light. The rms scatter around the best-fit relation is  $\sim 0.3$  dex,

but systematic errors could be as large, and the best-fit relation should be used with care. We have established a relationship between the parameterization of our template set for *ab*-type RR Lyrae stars and the results based on the Fourier expansion of light curves. This allowed us to estimate the metallicity from observed light curves with an estimated rms scatter of  $\sim 0.3$  dex. This method failed to uncover a systematic metallicity difference between field RR Lyrae stars and those associated with the Sgr stream, which is seen in main-sequence stars. Nevertheless, it is likely that this is a promising method for estimating metallicity, which is currently limited by the lack of a large and reliable calibration sample. Our templates can be used to bypass noisy Fourier transformation of sparsely sampled data, as already discussed by Kinemuchi et al. (2006) and Kovács & Kupi (2007).

We introduced a novel method for estimating metallicity that is based on the absolute magnitude versus metallicity relations for RR Lyrae stars and main-sequence stars (calibrated using globular clusters). This method does not require the *u*-band photometry, and will be useful to estimate the metallicity of spatially coherent structures that may be discovered by the Dark Energy and Pan-STARRS surveys. While the existing SDSS data are too shallow to apply this method to the Pisces stream, we used it to obtain a metallicity estimate for the Sgr tidal stream that is consistent with an independent estimate based on the photometric *u*-band method for main-sequence stars. Our result,  $[\text{Fe}/\text{H}] = -1.2$ , with an uncertainty of  $\sim 0.1$  dex, strongly rules out the hypothesis that the trailing arm of the Sgr dSph tidal stream has the same metallicity as halo field stars ( $[\text{Fe}/\text{H}] = -1.5$ ), as suggested by Watkins et al. (2009). Yanny et al. (2009) detected peaks at  $[\text{Fe}/\text{H}] = -1.3$  and at  $[\text{Fe}/\text{H}] = -1.6$  using SDSS spectroscopic metallicities for blue horizontal-branch (BHB) stars from the trailing arm. However, both the Yanny et al. and Watkins et al. results could be affected by systematic errors in the SDSS metallicity scale for BHB stars. Our results suggest that the SDSS metallicity scale for BHB stars could be biased low by about 0.3 dex (relative to the SDSS metallicity scale for main-sequence stars, and assuming that RR Lyrae and main-sequence stars from the Sgr tidal stream in stripe 82 area have the same metallicity distributions).

Simulations by Bullock & Johnston (2005) and Johnston et al. (2008) predict that there should be a difference in the chemical composition between stars in the inner halo that was built from accretion of massive satellites about 9 Gyr ago, and outer halo dominated by stars coming from dSph satellites that were accreted in the last 5 Gyr (see Figure 11 in Bullock & Johnston 2005). These accreted dSph satellites were presumably more metal-poor than the massive satellites accreted in earlier epochs (see Figure 3 in Robertson et al. 2005). Other recent simulation studies support these conclusions. For example, De Lucia & Helmi (2008) find evidence in their simulation for a strong concentration of (relatively) higher metallicity stars at distances close to the Galactic center, and the presence of (relatively) lower metallicity stars at distances beyond 20 kpc from the center. Zolotov et al. (2009) find from their simulations that their inner halos include stars from both in situ formed stars and accreted populations, while their outer halos appear to originate through pure accretion and disruption of satellites. Salvadori et al. (2009) have considered the distribution of ages and metallicities of metal-poor stars in a Milky-Way-like halo, as a function of galactocentric radius, based on a hybrid *N*-body and semianalytic simulation. They find an inner-halo population that is well described by a power-law index  $n = -3.2$  (for stars

with  $-2 < [\text{Fe}/\text{H}] < -1$ ), and an outer halo consistent with a much shallower profile,  $n = -2.2$ . The relative contributions of stars with  $[\text{Fe}/\text{H}] \leq -2$  in their simulation increases from about 16% for stars within  $7 \text{ kpc} < R < 20 \text{ kpc}$ , to  $> 40\%$  for stars with  $R > 20 \text{ kpc}$ .

Our observational results provide some support for these simulation-based predictions. The faintest main-sequence stars ( $r \sim 21.5$ ), not including those apparently associated with the Sgr stream, exhibit median metallicities at least 0.3 dex lower ( $[\text{Fe}/\text{H}] = -1.8$ , see the left panel in Figure 25) than halo stars within 10–15 kpc from the Galactic center (Ivezić et al. 2008). Other studies provide additional support. For example, Carollo et al. (2007, 2009) have indicated that field stars likely to be associated with the outer halo exhibit metallicities that are substantially lower ( $[\text{Fe}/\text{H}] = -2.2$ ) than those of the inner halo (they place the inner/outer halo boundary at  $\sim 10 \text{ kpc}$ ). The two metallicity measurements are fully consistent because photometric  $u$ -band metallicity estimator is biased high for spectroscopic values with  $[\text{Fe}/\text{H}] < -2$  (Bond et al. 2009).

Carollo et al. (2009) also found that the inferred density profiles of the inner- and outer-halo populations differ as well; the inner halo being consistent with a power-law profile with index  $n \sim -3.4$ , and the outer halo having index  $n = -2.1$  (the data analyzed by Carollo et al. are not suitable for determination of the relative normalizations of the inner- and outer-halo populations, due to the selection effects involved). This difference in the density profiles is very similar to the difference in density profiles for Oosterhoff I and Oosterhoff II stars. However, we emphasize that the steeper profile for the inner halo from Carollo et al. corresponds to more metal-rich stars, while we found weak evidence that Oosterhoff II stars tend to be more metal-poor than Oosterhoff I stars.

Simulations indicate that high surface brightness substructures in the halo originate from single satellites, typically massive dSph which tend to be accreted over the last few Gyr (Bullock & Johnston 2005), and these massive galaxies are expected to be more metal-rich than halo field stars (Font et al. 2008). The results from Ivezić et al. (2008) and the results presented here seem to support this prediction. The inner halo has a median metallicity of  $[\text{Fe}/\text{H}] = -1.5$ , while at least two strong overdensities have higher metallicities—the Monoceros stream has  $[\text{Fe}/\text{H}] = -1.0$ , and for the trailing part of the Sgr tidal stream we find  $[\text{Fe}/\text{H}] = -1.2$ . We emphasize that these three measurements are obtained using the same method/calibration and the same data set, and thus the measurements of relative differences are expected to be robust. Simulations by Johnston et al. (2008) predict that the metallicity of low surface brightness features, such as the Virgo Overdensity (Jurić et al. 2008), is expected to be lower than the median halo metallicity. Although the initial estimate by Jurić et al. (2008, see their Figure 39) claimed a metallicity for this structure of  $[\text{Fe}/\text{H}] \sim -1.5$ , a recent study of the photometric metallicity of stars in this structure by An et al. (2009) have suggested that the mean metallicity is even lower:  $[\text{Fe}/\text{H}] = -2.0$ . Both of these studies are limited by potentially large systematics associated with the photometric metallicity technique, so more detailed analysis of spectroscopically determined metallicities for stars in this structure would be of great value. The sparse information that is available, based on spectroscopic determinations, supports a mean metallicity between  $[\text{Fe}/\text{H}] = -1.8$  and  $-2.2$  (Duffau et al. 2006; Vivas et al. 2008; Prior et al. 2009; Casetti-Dinescu et al. 2009). Casetti-Dinescu et al. (2009) report the measurement of a precise absolute proper motion for the RR Lyrae star RR 167, which

appears highly likely to be associated with the Virgo Overdensity. This proper motion, in combination with their distance estimate (17 kpc from the Galactic center) and radial velocity measurement, indicate that the Virgo Overdensity structure may well be on a highly destructive orbit, with pericenter  $\sim 11 \text{ kpc}$ , and apocenter  $\sim 90 \text{ kpc}$ . Thus, the interpretation of the Virgo Overdensity as a dwarf galaxy, perhaps similar to those that participated in the formation of the outer-halo population, is strengthened.

Our result that (inner-) halo stellar number density profile steepens beyond  $\sim 30 \text{ kpc}$  is limited by the relatively small distance limit for main-sequence stars (35 kpc), the sparseness of the RR Lyrae sample ( $\sim 500$  objects), and the small survey area ( $\sim 300 \text{ deg}^2$ ). Ideally, the halo stellar number density profile should be studied using numerous main-sequence stars detected over a large fraction of sky. To do so to a distance limit of 100 kpc, imaging in at least  $g$  and  $r$  bands (or their equivalent) to a depth several magnitudes fainter than the co-added SDSS stripe 82 data is required ( $r > 25$ ). Pan-STARRS, the Dark Energy Survey and LSST are planning to obtain such data over large areas of sky. The LSST, with its deep  $u$ -band data, will also extend metallicity mapping of field main-sequence stars over half of the sky in the south; see Ivezić et al. (2008) for details. For substructures to be potentially discovered in the north by Pan-STARRS, the method presented here can be used to estimate the metallicity of spatially coherent structures even without the  $u$ -band data.

This research was supported in part by the National Science Foundation under grant PHY05-51164. B.S. and Ž.I. acknowledge support by NSF grants AST 61-5991 and AST 07-07901, and by NSF grant AST 05-51161 to LSST for design and development activity, and acknowledge the hospitality of the KITP at the University of California, Santa Barbara where part of this work was completed. Ž.I. acknowledges the hospitality of the Aspen Center for Physics. M.J. gratefully acknowledges support from the Taplin Fellowship, and NSF grants PHY-0503584 and AST-0807444. T.C.B. acknowledges partial support from PHY 08-22648: Physics Frontier Center/Joint Institute for Nuclear Astrophysics (JINA), awarded by the U.S. National Science Foundation. We are grateful to Kathy Vivas (CIDA) for helpful comments and discussions. Funding for the SDSS and SDSS-II has been provided by the Alfred P. Sloan Foundation, the Participating Institutions, the National Science Foundation, the U.S. Department of Energy, the National Aeronautics and Space Administration, the Japanese Monbukagakusho, the Max Planck Society, and the Higher Education Funding Council for England. The SDSS Web site is <http://www.sdss.org/>. The SDSS is managed by the Astrophysical Research Consortium for the Participating Institutions. The Participating Institutions are the American Museum of Natural History, Astrophysical Institute Potsdam, University of Basel, University of Cambridge, Case Western Reserve University, University of Chicago, Drexel University, Fermilab, the Institute for Advanced Study, the Japan Participation Group, Johns Hopkins University, the Joint Institute for Nuclear Astrophysics, the Kavli Institute for Particle Astrophysics and Cosmology, the Korean Scientist Group, the Chinese Academy of Sciences (LAMOST), Los Alamos National Laboratory, the Max-Planck-Institute for Astronomy (MPIA), the Max-Planck-Institute for Astrophysics (MPA), New Mexico State University, Ohio State University, University of Pittsburgh, University of Portsmouth, Princeton Univer-

sity, the United States Naval Observatory, and the University of Washington.

## REFERENCES

- Adelman-McCarthy, J. K., et al. 2008, *ApJS*, **175**, 297  
 Alcock, C., et al. 1996, *AJ*, **111**, 1146  
 An, D., et al. 2009, *ApJ*, **700**, 523  
 Arya, S., et al. 1998, *J. Assoc. Comput. Mach.*, **45**, 891  
 Bailey, S. I. 1903, *Science*, **18**, 593  
 Bell, E. F., et al. 2008, *ApJ*, **680**, 295  
 Belokurov, V., et al. 2006, *ApJ*, **642**, 137  
 Belokurov, V., et al. 2007a, *ApJ*, **658**, 337  
 Belokurov, V., et al. 2007b, *ApJ*, **657**, 89  
 Blanco, B. M. 1992, *AJ*, **103**, 1872  
 Blazhko, S. 1907, *Astron. Nachr.*, **175**, 325  
 Bond, N. A., et al. 2009, *ApJ*, submitted (arXiv:0909.0013)  
 Bramich, D. M., et al. 2008, *MNRAS*, **386**, 77  
 Bullock, J. S., & Johnston, K. V. 2005, *ApJ*, **635**, 931  
 Bullock, J. S., Kravtsov, A. V., & Weinberg, D. H. 2001, *ApJ*, **548**, 33  
 Cacciari, C., & Clementini, G. 2003, in *Stellar Candles for the Extragalactic Distance Scale*, ed. D. M. Alloin & W. Gieren (Springer Lecture Notes in Physics Vol. 635; Berlin: Springer), **105**  
 Cacciari, C., Corwin, T. M., & Carney, B. W. 2005, *AJ*, **129**, 267  
 Carollo, D., et al. 2007, *Nature*, **450**, 1020  
 Carollo, D., et al. 2009, *ApJ*, submitted (arXiv:0909.3019)  
 Casetti-Dinescu, D. I., et al. 2009, *ApJ*, **701**, 29  
 Catelan, M. 2009, *Ap&SS*, **320**, 261  
 De Lee, N. 2008, PhD thesis, Michigan State Univ.  
 De Lucia, G., & Helmi, A. 2008, *MNRAS*, **391**, 14  
 Dohm-Palmer, R. C., et al. 2001, *ApJ*, **555**, 37  
 Duffau, S., et al. 2006, *ApJ*, **636**, 97  
 Epstein, I., & Epstein, A. E. A. 1973, *AJ*, **78**, 83  
 Eyer, L., & Mowlavi, N. 2008, *J. Phys.: Conf. Ser.*, **118**, 2010  
 Font, A. S., et al. 2008, *ApJ*, **673**, 215  
 Freeman, K., & Bland-Hawthorn, J. 2002, *ARA&A*, **40**, 487  
 Frieman, J. A., et al. 2008, *AJ*, **135**, 338  
 Grillmair, C. J. 2006, *ApJ*, **645**, 37  
 Harding, P., et al. 2001, *AJ*, **122**, 1397  
 Helmi, A., & White, S. D. M. 1999, *MNRAS*, **307**, 495  
 Ibata, R. A., et al. 1997, *AJ*, **113**, 634  
 Ivezić, Ž., et al. 2000, *AJ*, **120**, 963  
 Ivezić, Ž., et al. 2003, *Mem. Soc. Astron. Italiana*, **74**, 978  
 Ivezić, Ž., et al. 2005, *AJ*, **129**, 1096  
 Ivezić, Ž., et al. 2007, *AJ*, **134**, 973  
 Ivezić, Ž., et al. 2008, *ApJ*, **684**, 287  
 Johnston, K. V., Hernquist, L., & Bolte, M. 1996, *ApJ*, **465**, 278  
 Johnston, K. V., et al. 2008, *ApJ*, **689**, 936  
 Jurcsik, J., & Kovács, G. 1996, *A&A*, **312**, 111  
 Jurić, M., et al. 2008, *ApJ*, **673**, 864  
 Kaiser, N., et al. 2002, *Proc. SPIE*, **4836**, 154  
 Keller, S. C., et al. 2008, *ApJ*, **678**, 851  
 Kinemuchi, K., et al. 2006, *AJ*, **132**, 1202  
 Kolenberg, K. 2008, *J. Phys.: Conf. Ser.*, **118**, 2060  
 Kovács, G., & Kupi, G. 2007, *A&A*, **462**, 1007  
 Kunder, A., & Chaboyer, B. 2008, *AJ*, **136**, 2441  
 Law, D. R., Johnston, K. V., & Majewski, S. R. 2005, *ApJ*, **619**, 807  
 Layden, A. C. 1994, *AJ*, **108**, 1016  
 Layden, A. C. 1998, *AJ*, **115**, 193  
 Lee, Y. S., et al. 2008, *AJ*, **136**, 2022  
 Lupton, R. H., et al. 2002, *Proc. SPIE*, **4836**, 350  
 Majewski, S. R., et al. 2003, *ApJ*, **599**, 1082  
 Marconi, M., et al. 2006, *MNRAS*, **371**, 1503  
 Mayer, L., et al. 2002, *MNRAS*, **336**, 119  
 Miceli, A., et al. 2008, *ApJ*, **678**, 865  
 Newberg, H. J., et al. 2002, *ApJ*, **569**, 245  
 Newberg, H. J., et al. 2003, *ApJ*, **596**, 191  
 Newberg, H. J., et al. 2007, *ApJ*, **668**, 221  
 Oosterhoff, P. T. 1939, *Observatory*, **62**, 104  
 Preston, G. W. 1959, *ApJ*, **130**, 507  
 Preston, G. W., Shectman, S. A., & Beers, T. C. 1991, *ApJ*, **375**, 121  
 Prior, S. L., et al. 2009, *ApJ*, **691**, 306  
 Reimann, J. D. 1994, PhD thesis, Univ. California, Berkeley  
 Robertson, B., et al. 2005, *ApJ*, **632**, 872  
 Salvadori, S., et al. 2009, *MNRAS*, submitted (arXiv:0908.4279)  
 Sandage, A. 2004, *AJ*, **128**, 858  
 Sandage, A., Katem, B., & Sandage, M. 1981, *ApJS*, **46**, 41  
 Schlaufman, K. C., et al. 2009, *ApJ*, **703**, 2177  
 Schlegel, D., Finkbeiner, D. P., & Davis, M. 1998, *ApJ*, **500**, 525  
 Sesar, B., et al. 2007, *AJ*, **134**, 2236 (S07)  
 Simon, N. R., & Clement, C. M. 1993, *ApJ*, **410**, 526  
 Smith, H. A. 1995, *RR Lyrae Stars* (Cambridge: Cambridge Univ. Press)  
 Sturch, C. 1966, *ApJ*, **143**, 774  
 Suntzeff, N. B., Kinman, T. D., & Kraft, R. P. 1991, *ApJ*, **367**, 528  
 Vivas, A. K., & Zinn, R. 2006, *AJ*, **132**, 714  
 Vivas, A. K., Zinn, R., & Gallart, C. 2005, *AJ*, **129**, 189  
 Vivas, A. K., et al. 2001, *ApJ*, **554**, 33  
 Vivas, A. K., et al. 2008, *AJ*, **136**, 1645  
 Watkins, L. L., et al. 2009, *MNRAS*, **398**, 1757  
 Wetterer, C. J., & McGraw, J. T. 1996, *AJ*, **112**, 1046  
 Yanny, B., et al. 2000, *ApJ*, **540**, 825  
 Yanny, B., et al. 2009, *ApJ*, **700**, 1282  
 York, D. G., et al. 2000, *AJ*, **120**, 1579  
 Zinn, R., & West, M. J. 1984, *ApJS*, **55**, 45  
 Zolotov, A., et al. 2009, *ApJ*, **702**, 1058